IOP Publishing Inverse Problems
Inverse Problems **30** (2014) 075007 (33pp) doi:10.1088/0266-5611/30/7/075007

A direct reconstruction method for anisotropic electrical impedance tomography

S J Hamilton, M Lassas and S Siltanen

Department of Mathematics & Statistics, University of Helsinki, Helsinki, Finland

E-mail: sarah.hamilton@helsinki.fi, matti.lassas@helsinki.fi and samuli.siltanen@helsinki.fi

Received 29 December 2013, revised 14 April 2014
Accepted for publication 29 April 2014
Published 25 June 2014

Abstract

A novel computational, non-iterative and noise-robust reconstruction method is introduced for the planar anisotropic inverse conductivity problem. The method is based on bypassing the unstable step of the reconstruction of the values of the isothermal coordinates on the boundary of the domain. Non-uniqueness of the inverse problem is dealt with by recovering the unique isotropic conductivity that can be achieved as a deformation of the measured anisotropic conductivity by *isothermal coordinates*. The method shows how isotropic D-bar reconstruction methods have produced reasonable and informative reconstructions even when used on EIT data known to come from anisotropic media, and when the boundary shape is not known precisely. Furthermore, the results pave the way for regularized anisotropic EIT. Key aspects of the approach involve D-bar methods and inverse scattering theory, complex geometrical optics solutions and quasi-conformal mapping techniques.

Keywords: electrical impedance tomography, anisotropic conductivity, D-bar method, quasi-conformal maps

(Some figures may appear in colour only in the online journal)

1. Introduction

A novel computational, non-iterative and noise-robust reconstruction method is introduced for the planar anisotropic inverse conductivity problem. The method is an extension of the so-called D-bar reconstruction methods used in isotropic EIT imaging, and is based on bypassing the unstable steps used in earlier anisotropic methods which involve derivatives of a highly unstable map. Numerical reconstructions from simulated anisotropic electrical impedance

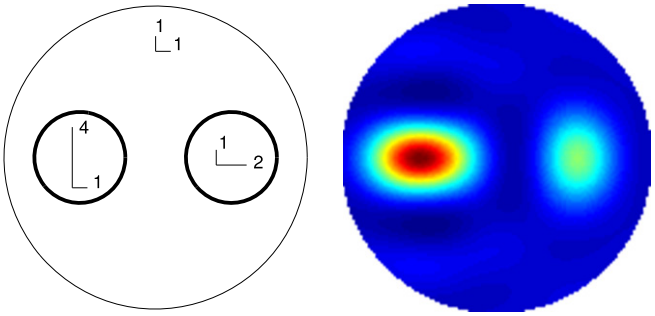

Figure 1. Left: anisotropic conductivity σ with two circular inclusions in an isotropic background. The strength and direction of the anisotropic preferences are indicated schematically. Right: reconstructed conductivity, which is isotropic and appropriately deformed. The anisotropic preferences squeeze the circular inclusions into ellipses.

tomography (EIT) data demonstrate that noise-robust images of isotropic, or scalar-valued, conductivities that are distorted versions of the original anisotropic conductivities can be reliably recovered.

EIT is a portable, inexpensive, non-invasive imaging modality which recovers the internal conductivity of a body using harmless electrical measurements taken at its surface. The reconstruction task is a highly ill-posed mathematical inverse problem whose goal is to produce images that can be used by a physician or engineer for diagnostic and evaluative purposes. Promising applications of EIT include monitoring heart and lung function in hospitalized patients [24, 32, 41, 42, 67], detection and classification of breast tumors [46–48, 77], and geophysical prospecting [3].

The vast majority of reconstruction techniques assume that the medium is isotropic, meaning that the electrical current will flow equally well in all directions. However, many bodies that are imaged are anisotropic: there is a spatially dependent preferred direction for current flow. For example, human heart tissue is three times more conductive along the muscle fibers than in the lateral directions [12]. There are relatively few reconstruction approaches designed for anisotropic cases, including [1, 2, 19, 33, 34, 63].

Another source of anisotropy is poorly known boundary shape: even if the conductivity is isotropic, incorrect modeling of the domain leads to EIT data that can only arise from an anisotropic conductivity distribution, in the incorrect model domain. The exact boundary shape is often impossible to obtain in practice as even by breathing, or reclining, a patient's chest shape can change significantly. (We remark that there are some techniques available for recovering the boundary shape from EIT data, see [25, 26, 56–59, 70, 71]. However, they assume the starting conductivity is isotropic.)

The main reason why the reconstruction literature concentrates on the isotropic case is the *non-uniqueness* of the anisotropic problem. In dimension 2, deforming the anisotropic conductivity by means of a boundary-fixing diffeomorphism does not change the EIT data, see [75] and [68, theorem 2]. Clearly, there exist uncountably many such deformations. In higher dimensions even less is known.

In our view, non-uniqueness should not be a show-stopper. Namely, even the isotropic inverse conductivity problem is so severely ill-posed that strong regularization is needed for robust image formation from noisy data. It is well-known from regularization theory [29], that in linear inverse problems non-uniqueness can be dealt with by picking out a unique representative from the same-data equivalence class, for example the one with minimal square

norm. In the nonlinear case of anisotropic EIT, we propose a non-iterative reconstruction method for two-dimensional (2D) anisotropic 2×2 conductivities σ that recovers the unique isotropic conductivity that can be achieved as a deformation of σ by *isothermal coordinates*. The method can recover useful information in a distorted form, as seen in figure 1.

Our starting point is the *D-bar methodology* for isotropic EIT. Rigorous mathematical analysis of the underlying physical problem has led to the development of direct (non-iterative) solution techniques, called D-bar methods, which employ inverse scattering theory to uniquely recover the isotropic conductivity. These methods have proven effective on simulated as well as experimental EIT data [7, 37, 42, 43, 72], and their regularization properties are well-understood [50]. They have even been used on human chest EIT data which is known to correspond to anisotropic tissues. The resulting images, while sometimes deformed, have nonetheless provided quality information [42].

We construct a combination of steps appearing in isotropic D-bar methods in such a way that

1. When applied to data arising from an anisotropic conductivity, the method recovers the above-mentioned unique isotropic conductivity (distorted).
2. When applied to data arising from an isotropic conductivity, the output of the new numerical method coincides with the standard D-bar reconstruction.

Our new method explains how isotropic D-bar reconstruction methods have produced reasonable and informative reconstructions even when used on EIT data known to come from anisotropic media and when the boundary shape is not known precisely. Furthermore, our results pave the way for regularized anisotropic EIT along the lines of the isotropic analysis given in [50].

The rest of the paper is organized as follows. Section 2 provides a brief review of the mathematical history of the isotropic and anisotropic EIT problems and lays out the proposed stable reconstruction method, proven in section 3. Section 4 describes the implementation details for the novel numerical algorithm obtained from the constructive proof given in section 3. The algorithm is tested on simulated finite element data for C^2 smooth, as well as discontinuous, anisotropic conductivities and the results are presented in section 5.

2. Mathematical history of the problem

2.1. History of the isotropic problem

The mathematical model for EIT, often called the *inverse conductivity problem* was introduced in Calderón's seminal paper [22] for isotropic conductivities γ. The voltage potential $u \in H^1(\Omega)$ inside a simply connected domain $\Omega \subset \mathbb{R}^n$ is the unique solution to the elliptic partial differential equation

$$\begin{aligned} &\nabla \cdot \gamma \nabla u = 0 \text{ in } (\Omega) \\ &u\big|_{\partial\Omega} = f \text{ on } \partial\Omega, \end{aligned} \tag{1}$$

with Dirichlet boundary condition defined by the applied voltage $f \in H^{1/2}(\partial\Omega)$, where ν is the outward facing unit normal vector to $\partial\Omega$. The domain Ω is a bounded simply connected set with a smooth boundary $\partial\Omega$ and the conductivity γ: $\Omega \to \mathbb{R}$ is a bounded measurable function satisfying $\gamma(x) \geqslant c > 0$ for almost every $x \in \Omega$. The isotropic inverse conductivity problem is then to recover the scalar-valued coefficient function $\gamma(x)$ from knowledge of the Dirichlet-to-Neumann (D–N) map

$$\Lambda_\gamma : f \mapsto \left. \gamma \frac{\partial u}{\partial \nu} \right|_{\partial\Omega}. \tag{2}$$

Physically, the D–N map is a voltage-to-current density map that describes the current flux at the boundary that results from an applied boundary voltage.

Calderón posited that any bounded isotropic conductivity γ could be uniquely determined using measurements taken at the boundary, i.e. the D–N map. The first major breakthrough towards this goal came in the 1987 paper of Sylvester and Uhlmann where they showed global uniqueness in dimensions 3 and greater for $\mathbb{C}^\infty$ conductivites [76]. In 1988, Nachman gave the first global constructive proof in dimensions $n \geqslant 3$ for $\partial\Omega \in C^{1,1}$ and $\gamma \in \mathbb{C}^{1,1}$. Both papers rely heavily on special solutions called *complex geometrical optics* (CGO) solutions, sometimes called *exponentially growing solutions*. Such solutions were originally introduced by Faddeev in 1966 [30] and rediscovered by Sylvester and Uhlmann. The constructive nature of Nachman's proof led to the formation of direct numerical D-bar algorithms by Knudsen *et al* [16, 17, 28, 51]. For further information about direct CGO methods in dimensions $n \geqslant 3$ see [17] and the references therein.

Breakthroughs in the 2D problem came in 1996 when Nachman [68] presented a constructive CGO based proof using a transformation to the Schrödinger equation, and in 2000 when Siltanen *et al* [72], using [68] as its backbone, developed the first numerical D-bar algorithm for twice-differentiable conductivities from D–N measurements and demonstrated its effectiveness on simulated data. In the approach, the isotropic conductivity γ is recovered by solving a $\overline{\partial}$ equation with non-physical scattering data defined by the D–N data. In 2009, Knudsen *et al* [50] showed that truncation of the scattering data (i.e. a low pass filtering) corresponds to a regularization strategy. The numerical D-bar algorithm has also proven effective in the experimental setting using measurements taken on physical electrodes [27, 42, 43]. We remark that one of the ways to reduce the computation time is to use either a Born approximation or a simpler Green's function to sidestep or simplify the first step in the D-bar algorithm (i.e. solving the boundary integral equation (BIE) for the traces of the CGO solutions). Such approaches were introduced in [72] and [65], and further examined in [4].

The regularity requirement was reduced to one derivative in 1997 in the constructive CGO proof by Brown and Uhlmann [20] based on a transformation to a first-order ∂ and $\overline{\partial}$ system (see also [15]). In 2003, Knudsen *et al* [49, 53] completed the proof of Brown and Uhlmann yielding the corresponding D-bar method and tested it on simulated data. In 2003, Astala and Päivärinta [9, 10] obtained the desired boundedness assumption $\gamma \in L^\infty(\Omega)$, thus solving Calderón's problem for planar conductivities, by using a constructive CGO proof based on a transformation to the Beltrami equation. The corresponding numerical algorithm was implemented in [7, 8].

In recent years, the complex isotropic coefficient γ problem in 2D has also been an emerging area of study. In 2000, Francini [31] extended the constructive results of Brown and Uhlmann to hold for γ such that $\mathrm{Re}(\gamma)$, $\mathrm{Im}(\gamma) \in W^{2,p}$ for some $p > 2$ where $\mathrm{Im}(\gamma)$ is small. The 2008 proof by Bukhgeim [21], strengthened by Blåsten [18], while not constructive in nature, answers the uniqueness question for smooth and complex 2D γ in the affirmative and does not require the smallness condition of [31]. Recently, the constructive CGO proof by Francini was completed by Hamilton *et al* [37] resulting in the first complex coefficient D-bar algorithm which has been demonstrated to work on simulated data [37, 38, 40] as well as experimental data.

The conditional stability of various reconstruction approaches for the inverse (isotropic) conductivity problem have been studied extensively [13, 14, 23, 64].

2.2. History of the anisotropic problem

If the conductivity is anisotropic, i.e. there is a spatially dependent preferred direction for the current to flow, then the conductivity is in fact a matrix-valued function $\sigma = [\sigma^{ij}(x)]$ where $1 \leqslant i, j \leqslant n$. The 2D anisotropic inverse conductivity problem is then to determine the matrix valued coefficient $\sigma(x)$ in the elliptic partial differential equation

$$\begin{aligned} &\nabla \cdot \sigma \nabla u = \sum_{i,j=1}^{2} \frac{\partial}{\partial x^i}\left[\sigma^{ij}(x)\right]\frac{\partial}{\partial x^j}u = 0 \text{ in } \Omega, \\ &u\big|_{\partial\Omega} = f, \end{aligned} \tag{3}$$

on a simply connected 2D domain $\Omega \subset \mathbb{R}^2$ with prescribed boundary voltage $f \in \mathcal{H}^{1/2}(\partial\Omega)$.

It is well known that for $\sigma(x) = [\sigma^{ij}(x)]$, $1 \leqslant i, j \leqslant 2$ a symmetric, positive-definite matrix function, that (3) has a unique solution $u \in H^1(\Omega)$. As $\sigma(x)$ is a symmetric positive-definite matrix, it can be written in terms of an eigen-decomposition $\sigma(x) = P^{-1}(x)\,D(x)\,P(x)$ where P is an orthogonal matrix whose rows are the eigenvectors of σ and D is a diagonal matrix comprised of the eigenvalues of σ. As σ is positive definite, the eigenvalues must be positive real values (a reality in realistic conductivities). In these terms, it is easy to see that the entries of σ can be expressed in the traditional basis $P = I$, the 2×2 identity matrix, for $\mathbb{R}^2$ where the entries of D then express the preferred direction and extent of the anisotropy of the tissue at a given point.

As in the isotropic case, one aims to recover the anisotropic conductivity from measurements taken only at the boundary. When σ and $\partial\Omega$ have some smoothness, the voltage-to-current density, or D–N, map can be defined as

$$\Lambda_\sigma(f) = Bu\,\big|_{\partial\Omega} = \nu \cdot \sigma \nabla u\big|_{\partial\Omega}, \tag{4}$$

where ν is the outward facing unit normal vector to $\partial\Omega$, $u \in H^1(\Omega)$ is the solution of (3), and f the prescribed voltage on $\partial\Omega$. Furthermore, by applying the Divergence theorem one finds

$$Q_{\sigma,\Omega}(\phi) := \int_\Omega \sum_{i,j=1}^{2} \sigma^{ij}(x)\frac{\partial u}{\partial x^i}\frac{\partial u}{\partial x^j}\mathrm{d}x = \int_{\partial\Omega} \Lambda_\sigma(\phi)\,\phi\,\mathrm{d}S(x), \tag{5}$$

which represents the power needed to maintain the voltage potential ϕ on $\partial\Omega$ where $dS(x)$ denotes the arc length on $\partial\Omega$. By the symmetry of Λ_σ, knowing $Q_{\sigma,\Omega}$ is equivalent to knowing Λ_σ.

Consider a diffeomorphism $F\colon \Omega \to \Omega$, $F(x) = (F^1(x), F^2(x))$, with $F|_{\partial\Omega} = \text{Identity}$. Making the change of variables $y = F(x)$ and setting $v = u \bigcirc F^{-1}$ in the first integral in (5), we obtain

$$\nabla \cdot \left(F_*\sigma\right)\nabla v = 0 \quad \text{in } \Omega,$$

where

$$\left(F_*\sigma\right)^{ij}(y) = \frac{1}{\det\left[\frac{\partial F^i}{\partial x^j}(x)\right]} \sum_{p,q=1}^{2} \frac{\partial F^i}{\partial x^p}(x)\frac{\partial F^j}{\partial x^q}(x)\sigma^{pq}(x)\Big|_{x=F^{-1}(y)}. \tag{6}$$

where F_* denotes the *push-forward* of the conductivity σ by the diffeomorphism F. Moreover, since F is the identity at $\partial\Omega$, (5) implies

$$\Lambda_{F_*\sigma} = \Lambda_\sigma.$$

Thus, the change of coordinates shows that there is a large class of conductivities which give rise to the same electrical measurements at the boundary, illustrating the non-uniqueness of the 2D anisotropic inverse problem.

The problem is thus not to recover the true anisotropic conductivity (as that is not possible) but rather to determine it up to the action of a class of diffeomorphisms. Sylvester [75], Sun and Uhlmann [74], and Astala *et al* [6] showed that there exists a unique isotropic conductivity $\gamma = \sqrt{\det \sigma}$, corresponding to the anisotropic conductivity σ under a quasi-conformal change of coordinates F (not necessarily preserving the boundary), such that

$$\Lambda_\gamma = \Lambda_{F_*\sigma},$$

for $\sigma \in C^3$, $\sigma \in W^{1,p}$, and $\sigma \in L^\infty$, respectively. Thus by solving the inverse anisotropic conductivity problem one can recover an isotropic representative for an equivalence class of anisotropic conductivities, i.e. an isotropization of the original conductivity.

In 2005, Astala *et al* [6] showed that it is possible to determine an L^∞ smooth anisotropic conductivity up to a $W^{1,2}$ diffeomorphism. Their result, while constructive in nature, requires the construction of the diffeomorphism F to determine the isotropic D–N map Λ_γ corresponding to the anisotropic D–N map Λ_σ, and then proceeds along the isotropic L^∞ approach of [10]. In particular, the *push forward* of the D–N map, i.e. $(F_{\partial\Omega})_*\Lambda_\sigma$ where $F_{\partial\Omega} = F|_{\partial\Omega}$: $\partial\Omega \to \partial\widetilde{\Omega}$, is constructed via

$$\left(F_{\partial\Omega}\right)_*\Lambda_\sigma : \widetilde{h} \mapsto \frac{\mathrm{d}F^{-1}_{\partial\Omega}}{\mathrm{d}\widetilde{x}}(\cdot)\left[\Lambda_\sigma\left(\widetilde{h} \bigcirc F_{\partial\Omega}\right)\right] \bigcirc \left(F_{\partial\Omega}\right)^{-1} \tag{7}$$

for functions $\widetilde{h} \in H^{1/2}(\partial\widetilde{\Omega})$. Even the determination of $F_{\partial\Omega}$ requires a large frequency limit of the anisotropic traces (see (54)), which from a numerical standpoint, is very unstable, especially in the presence of noise.

In dimensions $n \geqslant 3$ even less is known. Kohn and Vogelius [54, 55] showed that only piecewise analytic conductivities can be reconstructed, and for Riemannian manifolds the techniques have been generalized in [60–62].

2.3. The proposed approach

In this paper we build upon the theoretical anisotropic results of [6] and constructive isotropic proofs of [9, 10] and [68] to obtain a stable constructive CGO based proof, and related numerical reconstruction algorithm, for anisotropic C^2 conductivities that does not construct the unstable diffeomorphism F. We avoid the explicit construction of the map F by instead deriving a formula for the Beltrami scattering data (of [10]) in terms of the anisotropic CGO boundary traces (of [6]).

The reconstruction method from infinite-precision anisotropic D–N data consists of the following steps:

$$\begin{array}{c}\text{Anisotropic}\\ \text{D–N data}\\ \Lambda_\sigma\end{array} \xrightarrow{1} \begin{array}{c}\text{Anistropic}\\ \text{CGO traces}\end{array} \xrightarrow{2} \begin{array}{c}\text{Beltrami}\\ \text{scattering}\\ \text{data}\end{array} \xrightarrow{3} \begin{array}{c}\text{Schrödinger}\\ \text{scattering}\\ \text{data}\end{array} \xrightarrow{4} \begin{array}{c}\text{Isotropic}\\ \text{representative}\\ \gamma\end{array}.$$

We remark that Henkin and Santacesaria [39], have proposed an analogous reconstruction method based on Nachman's formulation, [68]. Our approach is based on the Astala–Päivärinta approach, and allows a lower level of regularity for the computation of the

scattering data in the reconstruction method. We then relate the isotropic (Beltrami) scattering data (for L^∞ conductivities) to the isotropic (Schrödinger) scattering data and the representative isotropic $W^{2,p}$-smooth conductivity $\gamma$is recovered using the D-bar method [72] based on Nachman's constructive proof [68].

In Steps 1–3 above, it is enough to require that $\sigma(z)$ and $\hat{\sigma} = \frac{\sigma(z)}{\det \sigma(z)}$ are in $L^\infty(\Omega)$ as the construction is based on Astala–Päivärinta technique [6, 9, 10]. The method proposed by Henkin and Santacesaria [39] results in a construction analogous to the Steps 1–3 for an anisotropic conductivity σ that is in $C^2(\overline{\Omega})$ and is isotropic near $\partial\Omega$. By instead using the Astala–Päivärinta approach for these steps, these regularity requirements are improved for the recovery of the scattering data.

In Step 4, numerical studies [11] indicate that discontinuous isotropic conductivities γ can be recovered when connecting the Beltrami and Schrödinger scattering data and solving the $\overline{\partial}_k$ equation of [68]. However, the theory is not yet complete. Therefore, in Step 4, we will assume that σ is in $W^{2,p}(\Omega)$, $p > 1$, and is the constant 1 near $\partial\Omega$.

We note that the assumptions that σ is equal to the constant 1 near $\partial\Omega$, and $\Omega = \mathbb{D}$ can be removed when conductivity and the boundary of the domain are assumed to be smoother. Indeed, if σ is in $C^3(\overline{\Omega})$ and the boundary $\partial\Omega$ is C^3-smooth, the functions equivalent to the boundary values of the determinant $\det(\sigma)|_{\partial\Omega}$ and its conormal derivative $\nu \cdot \sigma \nabla \det(\sigma)|_{\partial\Omega}$ can be uniquely determined using Λ_σ via explicit formulas (see [45]). Thus, if σ_0 is an anisotropic conductivity in $\Omega_0 \subset\subset \Omega$ that is $C^3(\overline{\Omega_0})$-smooth, $\partial\Omega_0$ is C^3-smooth, and we are given $\partial\Omega_0$ and Λ_{σ_0}, the construction can be started by reconstructing the functions $A_0 = \det(\sigma_0)|_{\partial\Omega_0}$ and $B_0 = \nu \cdot \sigma_0 \nabla \det(\sigma_0)|_{\partial\Omega_0}$. We can then construct, in $\Omega\backslash\Omega_0$, a $W^{2,p}(\Omega\backslash\Omega_0)$-smooth, $p > 1$, isotropic conductivity σ_1 such that σ_1 is one near $\partial\Omega$ and $\det(\sigma_1)|_{\partial\Omega_0} = A_0$ and $\nu \cdot \sigma_1 \nabla \det(\sigma_1)|_{\partial\Omega_0} = B_0$. We then define the conductivity σ in Ω which coincides with σ_0 in Ω_0 and σ_1 in $\Omega\backslash\Omega_0$. This conductivity may be only L^∞-smooth near $\partial\Omega_0$. However, this regularity is enough in Steps 1–3 above. One can compute the D–N map Λ_σ using Λ_{σ_0} and $\sigma|_{\Omega\backslash\Omega_0}$ (see [69, 73]). Here, we may assume that the domain Ω is a larger disc containing the original domain Ω_0. Numerically, this step involves some FEM solutions of intermediate D–N maps in the intermediate region, but such computations are less demanding than the solution of the D-bar equation.

Finally, the conductivity σ can be considered as a Riemannian metric in Ω, see [60–62]. Then, σ is piecewisely C^3-smooth in the Euclidean coordinates, we see that in the Riemannian boundary normal coordinates near $\partial\Omega_0$ it is $W^{2,p}$-smooth for all $p > 1$. Furthermore, when $F: \mathbb{R}^2 \to \mathbb{R}^2$ is the quasiconformal map that makes σ isotropic, we see that $F_*\sigma$ is an isotropic conductivity that is in $W^{2,p}_{loc}(\mathbb{R}^2)$, and hence it has the regularity needed in Step 4.

Summarizing, the assumptions that $\sigma \equiv 1$ near $\partial\Omega$and $\Omega = \mathbb{D}$ could in theory be removed. However, for simplicity, we require below that these assumptions aree valid.

3. The constructive CGO anisotropic proof

3.1. Preliminary considerations

In the following we identify $\mathbb{R}^2$ and $\mathbb{C}$ by the map $(x_1, x_2) \mapsto x_1 + ix_2$ and denote $z = x_1 + ix_2$. We use the standard notations

$$\partial_z = \frac{1}{2}\big(\partial_1 - i\partial_2\big), \quad \partial_{\bar{z}} = \frac{1}{2}\big(\partial_1 + i\partial_2\big),$$

where $\partial_j = \partial/\partial x_j$. For convenience, we work on the unit disc $\Omega = \mathbb{D} \subset \mathbb{R}^2$ but the results generalize to arbitrary domains. Below we consider σ: $\Omega \to \mathbb{R}^{2\times 2}$, with $\sigma = 1$ near $\partial\Omega$, to be extended as a function σ: $\mathbb{C} \to \mathbb{R}^{2\times 2}$ by defining $\sigma(z) = I$ for $z \in \mathbb{C}\backslash\Omega$. If $\Omega \subset \mathbb{R}^2$ is a bounded domain, it is convenient to consider the class of matrix functions $\sigma = [\sigma^{ij}]$ such that

$$\left[\sigma^{ij}\right] \in L^\infty\left(\Omega; \mathbb{R}^{2\times 2}\right), \quad \left[\sigma^{ij}\right]^t = \left[\sigma^{ij}\right], \quad C_0^{-1} I \leqslant \left[\sigma^{ij}\right] \leqslant C_0 I, \tag{8}$$

where $C_0 > 0$ and the superscript t denotes the non-conjugate matrix transpose. In this paper, the minimal possible value of C_0 is denoted by $C_0(\sigma)$. Note that it is necessary to require $C_0(\sigma) < \infty$, else there would be counterexamples showing that even the equivalence class of the conductivity cannot be recovered [35, 36].

For the symmetric positive-definite conductivity $\sigma = \sigma^{ij}$ we define the coefficient (see [10, 44, 75])

$$\widetilde{\mu}(z) = \frac{\sigma^{11}(z) - \sigma^{22}(z) + 2i\,\sigma^{12}(z)}{\sigma^{11}(z) + \sigma^{22}(z) + 2\sqrt{\det\big(\sigma(z)\big)}}, \tag{9}$$

which will serve as the Beltrami coefficient for the change of coordinates described below. The coefficient $\widetilde{\mu}(z)$ satisfies $|\widetilde{\mu}(z)| \leqslant \kappa < 1$ and is compactly supported.

Next we introduce a $W^{1,2}$-diffeomorphism (not necessarily preserving the boundary) that transforms the anisotropic conductivity into an isotropic one.

Lemma 3.1. *There is a quasiconformal homeomorphism F: $\mathbb{C} \to \mathbb{C}$ such that*

$$F(z) = z + \frac{A}{z} + O\left(\frac{1}{z^2}\right) = z + O\left(\frac{1}{z}\right) \quad \text{as } |z| \to \infty, \tag{10}$$

and such that $F \in W^{1,p}_{loc}\left(\mathbb{C}; \mathbb{C}\right)$, $2 < p < p\left(C_0\right) = \frac{2C_0}{C_0 - 1}$ for which

$$\left(F_*\sigma\right)(z) = \gamma(z) := \det\sqrt{\sigma\Big(F^{-1}(z)\Big)}\,. \tag{11}$$

Proof. The existence of such an F with $F(z) = z + O(1/z)$ is given in [6]. Here we make the asymptotics of F more precise.

The map F satisfies the following Beltrami equation

$$\overline{\partial}_z F(z) = \widetilde{\mu}(z)\,\partial_z F(z), \quad z \in \mathbb{C} \tag{12}$$

where $\widetilde{\mu}$ is given in (9). Define

$$G(z) = \frac{1}{F\left(\frac{1}{z}\right) - F(0)}. \tag{13}$$

As F: $\mathbb{C} \to \mathbb{C}$ is a homeomorphism, $F(z) = z + O(1/z)$, and $\overline{\partial}_z F(z) = 0$ for $|z| > 1$, $G(z)$ satisfies

$$\overline{\partial}_z G(z) = 0 \quad \text{in } \mathbb{D}\backslash\{0\}$$
$$\lim_{z\to 0} G(z) = \lim_{z\to 0} \frac{z}{1 + O(1) - zF(0)} = 0.$$

Therefore G has a removable singularity at $z = 0$, and if we define $G(0) = 0$, then the extended G satisfies

$$\overline{\partial}_z G(z) = 0 \quad \text{in } \mathbb{D},$$

and the expansion

$$G(z) = z + b_2 z^2 + b_3 z^3 + \cdots$$

holds near $z = 0$. Furthermore, $H(z) := z/G(z)$ is analytic in $B_\epsilon(0)$ as it is analytic in $B_\epsilon(0)\backslash\{0\}$ and bounded as $\lim_{z\to 0} \frac{z}{G(z)} = 1$, and thus

$$H(z) = \sum_{j=0}^{\infty} c_j z^j \quad \text{for } \left(|z| < \epsilon\right) \text{and } \left(c_0 = 1\right).$$

Now, from (13),

$$\begin{aligned} F(z) &= z\, H\left(\frac{1}{z}\right) + F(0) \\ &= z\left(1 + c_1 \frac{1}{z} + c_2 \frac{1}{z^2} + c_3 \frac{1}{z^3}\right) + F(0) \\ &= \left(c_1 + F(0)\right) + z + c_2 \frac{1}{z} + c_3 \frac{1}{z^2} + \cdots \\ &= z + \frac{A}{z} + O\left(\frac{1}{z^2}\right) \end{aligned}$$

for $|z| > \frac{1}{\epsilon}$, where $c_1 = -F(0)$ is dictated by the asymptotics of $F(z)$, and $c_2 = A$ is the sought-after constant, completing the proof.

Next we review the setup for the anisotropic problem described in [6]. In addition to the anisotropic conductivity equation (3), we consider the corresponding isotropic conductivity equation for $\gamma(\zeta) = (F_* \sigma)(\zeta)$ where $\zeta \in \widetilde{\Omega} = F(\Omega)$. For these considerations, we observe that if u satisfies equation (3) and γ is as in (11) then the function

$$w(\zeta) = u\left(F^{-1}(\zeta)\right) \in H^1\left(\widetilde{\Omega}\right),$$

satisfies the isotropic conductivity equation

$$\begin{aligned} &\nabla \cdot \gamma \nabla w = 0 \quad \text{in } \widetilde{\Omega}, \\ &w\big|_{\partial\widetilde{\Omega}} = \phi \circ F^{-1}. \end{aligned} \tag{14}$$

Thus, γ can be considered as a scalar, isotropic L^∞ smooth conductivity γI. We also extend the isotropic function γ: $\widetilde{\Omega} \to \mathbb{R}_+$ to a function γ: $\mathbb{C} \to \mathbb{R}_+$ by defining $\gamma(\zeta) = 1$ for $\zeta \in \mathbb{C}\backslash\widetilde{\Omega}$.

While solving the isotropic inverse problem in [10], the interplay between the scalar conductivities $\gamma(\zeta)$ and $\frac{1}{\gamma(\zeta)}$ played a crucial role. Motivated by this, we define

$$\hat{\sigma}^{ij}(z) = \frac{1}{\det\big(\sigma(z)\big)}\sigma^{ij}(z), \quad z \in \mathbb{C},$$

for the anisotropic conductivity σ. Note that for an isotropic conductivity σ, this would reduce to $\hat{\sigma} = 1/\sigma$.

Now let F be the quasiconformal map defined in lemma 3.1 and $\gamma = F_*\sigma$ as in (11). We say that $\widehat{w} \in H^1(\widetilde{\Omega})$ is a γ-harmonic conjugate of w if

$$\begin{aligned} \partial_1\widehat{w}\big(\zeta\big) &= -\gamma(z)\,\partial_2 w\big(\zeta\big), \\ \partial_2\widehat{w}\big(\zeta\big) &= \gamma(z)\,\partial_1 w\big(\zeta\big), \end{aligned} \tag{15}$$

where $\zeta \in \widetilde{\Omega}$. Using $\widehat{w}$, we define the function $\hat{u}$, which we call the σ-harmonic conjugate of u,

$$\hat{u}(z) = \widehat{w}\big(F(z)\big).$$

To determine the equation governing $\hat{u}$, it easily follows that (cf [10])

$$\nabla \cdot \frac{1}{\gamma}\nabla\widehat{w} = 0 \quad \text{in } \widetilde{\Omega}, \tag{16}$$

and by changing the coordinates to $\zeta = F(z)$ we see that $1/\gamma = F_*\hat{\sigma}$. These facts imply

$$\nabla \cdot \hat{\sigma}\,\nabla\hat{u} = 0 \quad \text{in } \Omega. \tag{17}$$

Thus, $\hat{u}$ is the $\hat{\sigma}$-harmonic conjugate function of u and we have

$$\nabla\hat{u} = J\sigma\,\nabla u, \qquad \nabla u = J\hat{\sigma}\,\nabla\hat{u}, \qquad \text{where } J = \begin{pmatrix} 0 & -1 \\ 1 & 0 \end{pmatrix}. \tag{18}$$

Since u is a solution to the conductivity equation if and only if $u + c$ (where $c \in \mathbb{C}$) is a solution, we see from (18) that the Cauchy data pairs C_σ determine the pairs $C_{\hat{\sigma}}$ and vice versa. Thus we get, almost for free, that Λ_σ determines $\Lambda_{\hat{\sigma}}$, as well.

Lemma 3.2 and corollary 3.3 of [6] describe the relationship between the anisotropic conductivity equations

$$\nabla \cdot \sigma\,\nabla u = 0, \qquad \text{and} \qquad \nabla \cdot \hat{\sigma}\,\nabla\hat{u} = 0, \quad z \in \mathbb{C},$$

and the anisotropic Beltrami equation for σ, for fixed $k \in \mathbb{C}$,

$$\begin{aligned} &\overline{\partial}_z g(z) = \mu_1(z)\,\partial_z g(z) + \mu_2(z)\,\overline{\partial_z g(z)}, \quad z \in \mathbb{C} \\ &g\big(z, k\big) = e^{ikz}\left(1 + O_k\left(\frac{1}{|z|}\right)\right), \end{aligned} \tag{19}$$

for $g = u + i\hat{u}$ and the scalar Beltrami coefficients μ_1 and μ_2 defined by

$$\mu_1 = \frac{\sigma^{22} - \sigma^{11} - 2i\sigma^{12}}{1 + \operatorname{tr}(\sigma) + \det(\sigma)}, \qquad \text{and} \qquad \mu_2 = \frac{1 - \det(\sigma)}{1 + \operatorname{tr}(\sigma) + \det(\sigma)}. \tag{20}$$

Note that $O_k(h(z))$ denotes a function of (z,k) that satisfies

$$\big|O_k\big(h(z)\big)\big| \leqslant C\big(k\big)\big|h(z)\big|, \quad \forall\, z \in \mathbb{C},$$

where $C(k)$ is a constant depending only on $k \in \mathbb{C}$. We will also make use of the Beltrami system for $\hat{\sigma}$

$$\overline{\partial}_z \widetilde{g}(z) = \mu_1(z)\,\partial_z \widetilde{g}(z) - \mu_2(z)\,\overline{\partial_z \widetilde{g}(z)}, \quad z \in \mathbb{C}$$
$$\widetilde{g}(z, k) = e^{ikz}\left(1 + O_k\left(\frac{1}{|z|}\right)\right), \tag{21}$$

resulting from using $\hat{\sigma}$ in (19). Here μ_1 and μ_2 are as defined above in (20) in terms of σ.

From [6], the boundary values of u and $\hat{u}$ are related by

$$\tau \cdot \nabla \hat{u}\big|_{\partial\Omega} = \Lambda_\sigma\big(u|_{\partial\Omega}\big),$$

or equivalently,

$$\partial_T \hat{u} = \Lambda_\sigma(u), \quad \text{for z} \in \partial\Omega, \tag{22}$$

where $T = (-\nu_2, \nu_1)$ is the unit tangent vector to $\partial\Omega$ and thus ∂_T denotes the tangential derivative on $\partial\Omega$ in the counter-clockwise direction. We define the σ-Hilbert transform by

$$\mathcal{H}_\sigma\colon H^{1/2}(\partial\Omega) \to H^{1/2}(\partial\Omega)/\mathbb{C}$$
$$\text{Re } g|_{\partial\Omega} \mapsto \text{Im } g|_{\partial\Omega} + \mathbb{C}. \tag{23}$$

Note that if $\text{Re } g|_{\partial\Omega} = u|_{\partial\Omega}$ and $\text{Im } g|_{\partial\Omega} = \hat{u}|_{\partial\Omega}$, then the σ-Hilbert transform $\mathcal{H}_\sigma$ connects the function u and it's $\hat{\sigma}$-conjugate function $\hat{u}$ by

$$\mathcal{H}_\sigma(u) = \hat{u}. \tag{24}$$

By taking the tangential derivative and (22) we have

$$\partial_T\big(\mathcal{H}_\sigma(u)\big) = \Lambda_\sigma u, \tag{25}$$

and thus, as in [9], we see that Λ_σ determines the σ-Hilbert transform $\mathcal{H}_\sigma$ defined by (23) and the σ-Hilbert transform is essentially just a reformulation of the D–N map Λ_σ.

From [6, lemma 3.4] we have the following lemma involving the anisotropic D–N maps Λ_σ and $\Lambda_{\hat{\sigma}}$:

Lemma 3.2. *The D–N map Λ_σ determines the maps $\Lambda_{\hat{\sigma}}$ and $\mathcal{H}_\sigma$.*

3.2. The non-linear isotropic Beltrami scattering transform

Next we review the scattering data for the $\overline{\partial}_k$ equation related to the isotropic Beltrami equation [9, 10], in our setting. Let

$$u_\gamma(\zeta, k) = \text{Re}\, f_{\mu_\gamma}(\zeta, k) + i\,\text{Im}\, f_{-\mu_\gamma}(\zeta, k), \tag{26}$$

where $f_{\pm\mu_\gamma}$ are the CGO solutions to the following isotropic Beltrami equations, for fixed $k \in \mathbb{C}$,

$$\overline{\partial}_\zeta f_{\pm\mu_\gamma}(\zeta, k) = \pm\ \mu_\gamma(\zeta)\,\overline{\partial_\zeta f_{\pm\mu_\gamma}(\zeta, k)}, \quad \zeta \in \mathbb{C}$$
$$f_{\pm\mu_\gamma}(\zeta, k) = e^{ik\zeta}\left(1 + O_k\left(\frac{1}{|\zeta|}\right)\right), \tag{27}$$

where

$$\mu_\gamma(\zeta) = \frac{1-\gamma(\zeta)}{1+\gamma(\zeta)}, \qquad -\mu_\gamma(\zeta) = \frac{1-1/\gamma(\zeta)}{1+1/\gamma(\zeta)}, \tag{28}$$

are the corresponding Beltrami coefficients for the isotropic conductivity $\gamma(\zeta) = (F_*\sigma)(\zeta)$ and $1/\gamma(\zeta) = (F_*\hat{\sigma})(\zeta)$, respectively. Here σ denotes the original anisotropic conductivity, and $F\colon \mathbb{C} \to \mathbb{C}$ the unique diffeomorphism whose *push-forward* of $\sigma(z)$ is the isotropic conductivity $\gamma(\zeta)$, with asymptotic condition as in lemma 3.1.

As $\gamma(\zeta) \equiv 1$ for $\zeta \in \mathbb{C}\backslash\widetilde{\Omega}$, we have $\mu_\gamma(\zeta) = 0$ and thus $f_{\pm\mu_\gamma}(\zeta, k)$ are analytic in $\zeta$for $\zeta \in \mathbb{C}\backslash\widetilde{\Omega}$. Writing

$$f_{\pm\mu_\gamma}(\zeta, k) = e^{ik\zeta} M_\gamma^{\pm}(\zeta, k), \tag{29}$$

where

$$M_\gamma^{\pm}(\zeta, k) = 1 + O_k\left(\frac{1}{|\zeta|}\right), \quad |\zeta| \to \infty, \tag{30}$$

we see that $M_\gamma^{\pm}(\zeta, k)$ are also analytic for $\zeta \in \mathbb{C}\backslash\widetilde{\Omega}$, and thus admit power series representations

$$M_\gamma^{\pm}(\zeta, k) = \sum_{n=0}^{\infty} \frac{b_n^{\pm}(k)}{\zeta^n} = b_0^{\pm}(k) + \frac{b_1^{\pm}(k)}{\zeta^1} + \frac{b_2^{\pm}(k)}{\zeta^2} + \frac{b_3^{\pm}(k)}{\zeta^3} + \cdots, \tag{31}$$

for $|z| > R$ large, and that $b_0^{\pm}(k) = 1$ from the large $|\zeta|$ asymptotics of $M_\gamma^{\pm}$ given in (30). Note that $b_n^{\pm}(k)$ denote the coefficients in the expansion and depend on the scattering parameter $k \in \mathbb{C}$.

Using this expansion for $M_\gamma^{\pm}(\zeta, k)$ in the formulation of $f_{\pm\mu_\gamma}(\zeta, k)$, we see

$$\begin{aligned} f_{\pm\mu_\gamma}(\zeta, k) &= e^{ik\zeta}\left(1 + \sum_{n=1}^{\infty} \frac{b_n^{\pm}(k)}{\zeta^n}\right) \\ &= e^{ik\zeta} + \frac{b_1^{\pm}(k)}{\zeta^1} e^{ik\zeta} + \frac{b_2^{\pm}(k)}{\zeta^2} e^{ik\zeta} + \frac{b_3^{\pm}(k)}{\zeta^3} e^{ik\zeta} + \cdots, \end{aligned} \tag{32}$$

for $|\zeta| > R$. By construction, $u_\gamma(\zeta, k) = \operatorname{Re} f_{\mu_\gamma}(\zeta, k) + i \operatorname{Im} f_{-\mu_\gamma}(\zeta, k)$ is a solution to the isotropic conductivity equation

$$\nabla \cdot \gamma(\zeta) \nabla u_\gamma(\zeta, k) = 0. \tag{33}$$

From [5, (18.34)], u_γ satisfies the following D-bar equation in the auxiliary variable k

$$\overline{\partial}_k u_\gamma(\zeta, k) = -i\tau(k)\overline{u_\gamma(\zeta, k)}, \quad \zeta \in \mathbb{C}, \tag{34}$$

where

$$\tau(k) = \frac{1}{2}\left(\overline{b_1^+(k)} - \overline{b_1^-(k)}\right), \tag{35}$$

plays the role of the non-physical scattering data, and $b_1^{\pm}(k)$ are coefficients in the large $|\zeta|$ expansion (31).

Notice that $\tau(k)$ is independent of the spatial coordinates, only requiring $|\zeta|$ large to compute the coefficients $b_1^{\pm}(k)$. This will play an important role in relating the

anisotropic and isotropic Beltrami problems. This scattering data $\tau(k)$, for L^∞ isotropic conductivities, is related to the scattering data $\mathbf{t}(k)$ of [68] for C^2 smooth conductivities via [8]

$$\mathbf{t}(k) = -4\pi i\bar{k}\tau(k),$$

which we will use to avoid forming the unstable coordinate deformation map F. Next we define the scattering data $\tau(k)$ in terms of the measured anisotropic boundary data.

3.2.1. BIEs for the scattering data. We now seek to relate the anisotropic and isotropic CGO solutions, in a similar manner as [6], in order to evaluate the isotropic Beltrami scattering transform $\tau(k)$ in terms of the anisotropic Beltrami CGOs. We briefly review the setting here.

We seek CGO solutions $W_\sigma^+(z, k)$ for $k \in \mathbb{C}$ and $z \in \mathbb{C}\backslash\mathbb{D}$ for the anisotropic σ problem satisfying

$$\bar{\partial}_z W_\sigma^+(z, k) = 0, \quad \text{for}(z \in \mathbb{C}\backslash\mathbb{D}), \tag{36}$$

$$W_\sigma^+(z, k) = e^{ikz}\left(1 + O_k\left(\frac{1}{|z|}\right)\right), \tag{37}$$

$$\text{Im}\ \ W_\sigma^+(z, k)\big|_{z\in\partial\mathbb{D}} = \mathcal{H}_\sigma\left(\text{Re}\ \ W_\sigma^+(z, k)\big|_{z\in\partial\mathbb{D}}\right). \tag{38}$$

Such solutions correspond to the restriction of the CGO solutions $g(z, k)$ of the anisotropic conductivity equation (19) to the exterior domain $\mathbb{C}\backslash\mathbb{D}$, i.e. $W_\sigma^+(\cdot, k) = g(\cdot, k)|_{\mathbb{C}\backslash\mathbb{D}}$. There $\sigma = I$, the 2×2 identity matrix, and thus $\mu_1(z) = 0 = \mu_2(z)$ for $|z| \geqslant 1$ and hence $W_\sigma^+(z, k)$ is harmonic in $\mathbb{C}\backslash\mathbb{D}$.

For the isotropic conductivity problem, we seek CGO solutions $W_\gamma^+(\zeta, k)$ for $k,\ \zeta \in \mathbb{C}$ satisfying the isotropic Beltrami problem

$$\bar{\partial}_\zeta W_\gamma^+(\zeta, k) = \mu_\gamma(\zeta)\overline{\partial_\zeta W_\gamma^+(\zeta, k)}, \quad \zeta \in \mathbb{C} \tag{39}$$

$$W_\gamma^+(\zeta, k) = e^{ik\zeta}\left(1 + O_k\left(\frac{1}{|\zeta|}\right)\right). \tag{40}$$

Similarly for the $\hat{\sigma}$ anisotropic and $1/\gamma$ isotropic problems we desire CGO solutions $W_\sigma^-(z, k)$ and $W_\gamma^-(\zeta, k)$, respectively, such that

$$\bar{\partial}_z W_\sigma^-(z, k) = 0, \quad \text{for}(z \in \mathbb{C}\backslash\mathbb{D}), \tag{41}$$

$$W_\sigma^-(z, k) = e^{ikz}\left(1 + O_k\left(\frac{1}{|z|}\right)\right), \tag{42}$$

$$\text{Im}\ \ W_\sigma^-(z, k)\big|_{z\in\partial\mathbb{D}} = \mathcal{H}_{\hat{\sigma}}\left(\text{Re}\ \ W_\sigma^-(z, k)\big|_{z\in\partial\mathbb{D}}\right), \tag{43}$$

where $W_\sigma^-(z, k)$ is the restriction of $\tilde{g}(z, k)$ from (21) to the exterior domain $\mathbb{C}\backslash\mathbb{D}$, i.e. $W_\sigma^-(\cdot, k) = g(\cdot, k)\big|_{\mathbb{C}\backslash\mathbb{D}}$, and

$$\bar{\partial}_\zeta W_\gamma^-(\zeta, k) = -\mu_\gamma(z)\overline{\partial_\zeta W_\gamma^-(\zeta, k)}, \quad \zeta \in \mathbb{C} \tag{44}$$

$$W_\gamma^-(\zeta, k) = e^{ik\zeta}\left(1 + O_k\left(\frac{1}{|\zeta|}\right)\right). \tag{45}$$

Recall that by the definition of $\mu_\gamma(\zeta, k) = \frac{1-\gamma(\zeta)}{1+\gamma(\zeta)}$, the isotropic CGO solutions $W_\gamma^\pm(\zeta, k)$ are harmonic in ζ for $\zeta \in \mathbb{C}\backslash\widetilde{\Omega}$. The CGO solutions to the anisotropic and isotropic problems in the exterior domain are closely related via a change of coordinates. The following lemma, from [6], Lemma 3.5], clarifies the relation and is stated for W_σ^+ and W_γ^+. The result also holds for W_σ^- and W_γ^- using the same map F.

Lemma 3.3. *For all $k \in \mathbb{C}$ we have:*

(i) The system (39)–(40) has a unique solution $W_\gamma^+(\zeta, k)$ for $\zeta \in \mathbb{C}$.

(ii) The system (37)–(38) has a unique solution $W_\sigma^+(z, k)$ for $z \in \mathbb{C}\backslash\mathbb{D}$.

(iii) For $z \in \mathbb{C}\backslash\mathbb{D}$, we have

$$W_\sigma^+(z, k) = W_\gamma^+(F(z), k), \tag{46}$$

where $F\colon \mathbb{C} \to \mathbb{C}$ denotes the diffeomorphism such that $(F_*\sigma)(z) = \gamma(z)$ described in lemma 3.1.

Above we saw that the scattering transform $\tau(k)$ is independent of the spatial coordinates. We will now use lemma 3.3 to derive a BIE for the scattering transform $\tau(k)$ in terms of the boundary traces of the anisotropic CGO solutions, thus providing the crucial connection between our anisotropic data in the *physical space*, and the isotropic version in the *virtual space* (isothermal coordinates).

Let $W_\gamma^\pm(\zeta, k) = f_{\pm\mu_\gamma}(\zeta, k)$, for $k,\ \zeta \in \mathbb{C}$. By lemma 3.3 part (iii) we have, in the exterior domain,

$$W_\sigma^\pm(z, k) = W_\gamma^\pm(F(z), k) = f_{\pm\mu_\gamma}(F(z), k), \qquad z \in \mathbb{C}\backslash\mathbb{D}.$$

As F is a quasiconformal homeomorphism and diffeomorphism with asymptotics given in (10), for $|F(z)| > R$ we can use the power series representation for $f_{\pm\mu_\gamma}(z, k)$ from (32)

$$\begin{aligned} W_\sigma^\pm(z, k) &= f_{\pm\mu_\gamma}(F(z), k) \\ &= e^{ikF(z)}\left[1 + \frac{b_1^\pm(k)}{F(z)} + \frac{b_2^\pm(k)}{(F(z))^2} + \cdots\right]. \end{aligned} \tag{47}$$

Using the first-order development of $F(z)$ in lemma 3.1, from (10)

$$F(z) = z + \frac{A}{z} + O\left(\frac{1}{|z|^2}\right),$$

we see

$$\begin{aligned} W_\sigma^\pm(z,k) &= e^{ikF(z)}\left[1 + \frac{b_1^\pm(k)}{F(z)} + \frac{b_2^\pm(k)}{(F(z))^2} + \cdots\right] \\ &= e^{ikz}\left[1 + \frac{ikA + b_1^\pm(k)}{z} + O_k\left(\frac{1}{|z|^2}\right)\right] \\ &= e^{ikz}\left[1 + \frac{\widetilde{b}_1^\pm(k)}{z} + O_k\left(\frac{1}{|z|^2}\right)\right], \end{aligned} \tag{48}$$

where

$$\widetilde{b}_1^\pm(k) = ikA + b_1^\pm(k). \tag{49}$$

We can express the scattering transform $\tau(k)$ in terms of the new coefficient $\widetilde{b}_1^\pm(k)$ as follows:

$$\tau(k) = \frac{1}{2}\left(\overline{b_1^+(k)} - \overline{b_1^-(k)}\right) = \frac{1}{2}\left(\overline{\widetilde{b}_1^+(k)} - \overline{\widetilde{b}_1^-(k)}\right), \tag{50}$$

as the constant A cancels. Thus we have related the isotropic Beltrami scattering transform to the anisotropic CGOs.

Next, we will derive BIEs for the coefficients $\widetilde{b}_1^\pm(k)$, and thus the isotropic Beltrami scattering transform $\tau(k)$, in terms of the boundary traces of the anisotropic Beltrami CGOs $M_\sigma^\pm$. Recall that $M_\sigma^\pm(z,k)$ are analytic for $|z| \geqslant 1$, and from (48) we have

$$\begin{aligned} M_\sigma^\pm(z,k) &= e^{-ikz}W_\sigma^\pm(z,k) \\ &= e^{-ikz}f_{\pm\mu_\gamma}(F(z),k) \\ &= 1 + \frac{\widetilde{b}_1^\pm(k)}{z} + O_k\left(\frac{1}{|z|^2}\right), \quad |z| \to \infty \end{aligned} \tag{51}$$

Now, let

$$\begin{aligned} h(z,k) &= \frac{1}{z}M_\sigma^\pm\left(\frac{1}{z},k\right) - \frac{1}{z} \\ &= \frac{1}{z}\left[1 + \widetilde{b}_1^\pm(k)z + O_k\left(|z|^2\right)\right] - \frac{1}{z} \\ &= \widetilde{b}_1^\pm(k) + O_k\left(|z|\right), \quad |z| \to 0. \end{aligned} \tag{52}$$

By definition, $h(z,k)$ is analytic in z for $z \in \mathbb{D}\backslash\{0\}$. In fact, as $h(z,k)$ is bounded, we know that $h(z,k)$ is analytic at $z = 0$ as well and thus by setting $h(0,k) = \widetilde{b}_1^\pm(k)$, we extend $h(z,k)$ to all of $\mathbb{D}$. By the Cauchy Integral Formula, the value of $h(z,k)$ for any $|z| < 1$ is completely determined by the values at the boundary, and thus

$$\begin{aligned}\widetilde{b}_1^{\pm}(k) &= h(0, k)\\ &= \frac{1}{2\pi i}\int_{\partial\mathbb{D}} \frac{h(z, k)}{z-0}\, dz\\ &= \frac{1}{2\pi i}\int_{\partial\mathbb{D}} \frac{1}{z-0}\left[\frac{1}{z} M_\sigma^{\pm}\left(\frac{1}{z}, k\right) - \frac{1}{z}\right] \mathrm{d}z\\ &= \frac{1}{2\pi i}\int_{\partial\mathbb{D}} \frac{1}{z^2}\left[M_\sigma^{\pm}\left(\frac{1}{z}, k\right) - 1\right] \mathrm{d}z,\end{aligned}$$

or equivalently,

$$\widetilde{b}_1^{\pm}(k) = \frac{1}{2\pi i}\int_{\partial\mathbb{D}} \left(M_\sigma^{\pm}(z, k) - 1\right) \mathrm{d}z. \tag{53}$$

Thus, we can determine the scattering transform $\tau(k)$ using the traces of the CGO solutions $M_\sigma^{\pm}(z, k)$ to the anisotropic problem, in the physical coordinates, resulting in the following theorem which holds for anisotropic σ, and $\hat{\sigma} \in L^\infty$.

Theorem 3.4. *The Beltrami scattering transform data $\tau(k)$ for the isotropic conductivity $\gamma = F_*\sigma$, where F is as in lemma 3.1, can be calculated in terms of the boundary values of the anisotropic σ and $\hat{\sigma}$ Beltrami CGO solutions via*

$$\tau(k) = \frac{\overline{\widetilde{b}_1^{+}(k)} - \overline{\widetilde{b}_1^{-}(k)}}{2},$$

where

$$\widetilde{b}_1^{\pm}(k) = \frac{1}{2\pi i}\int_{\partial\mathbb{D}} \left[M_\sigma^{\pm}(z, k) - 1\right] \mathrm{d}z.$$

Proof. The proof follows directly from (50) and (53). □

3.2.2. From scattering data to isotropic conductivity $\gamma = \sqrt{\det\sigma}$. As the scattering transform $\tau(k)$ is independent of the spatial coordinates, we can now proceed with the established theory for the isotropic conductivity problem. Following along the L^∞ approach of [10] would require knowledge of the isotropic CGO solutions $M_\gamma^{\pm}$ in the exterior domain $\mathbb{C}\backslash\widetilde{\Omega}$ and thus the explicit formation of the unstable map F at the boundary $\partial\widetilde{\Omega} = F(\partial\Omega)$ via [6]

$$F(z) = \lim_{k\to\infty} \frac{\log W_\sigma^{+}(z, k)}{ik}, \quad z \in \mathbb{C}\backslash\Omega. \tag{54}$$

Note that the logarithm is not necessarily the principal branch. For any $k \neq 0$ we consider the logarithm of $G(z, k) = W_\sigma^{+}(F(z), k)$ where the branch is chosen so that $\log G(z, k)$ is a continuous function of $z \in \mathbb{C}\backslash\Omega$ and $\lim_{z\to\infty}(\log G(z, k) - ikz) = 0$. Then one has $\lim_{k\to\infty} \frac{\log G(z,k)}{ik} = F(z)$. Note that such a choice of the branch of the logarithm is not numerically feasible as one would need to compute values of $G(z, k)$ for both large z and k, when we only have the boundary traces for small magnitude k.

Instead, we bypass constructing the map F completely by relating the L^∞ isotropic Beltrami scattering transform $\tau(k)$ to the C^2 isotropic Schrödinger scattering transform $\mathbf{t}(k)$ via [8]

$$\mathbf{t}(k) = -4\pi i\bar{k}\tau(k), \tag{55}$$

and continue by solving the C^2 isotropic conductivity problem [68]. Therefore, for each fixed $\zeta \in \widetilde{\Omega}$, we solve the following $\overline{\partial}_k$ equation

$$\overline{\partial}_k \mathcal{M}(\zeta, k) = \frac{1}{4\pi\overline{k}} \mathbf{t}(k)\, e(\zeta, -k)\, \overline{\mathcal{M}(\zeta, k)}, \tag{56}$$

for $\mathcal{M}(\zeta, k)$, $k \in \mathbb{C}$, where $e(\zeta, k) := \exp(i(k\zeta + \overline{k}\overline{\zeta}))$ is a unimodular multiplier. Here $\mathcal{M}(\zeta, k)$ are the CGO solutions of Nachman [68], and $\mathcal{M}(\zeta, k) - 1 \in W^{1,\widetilde{p}}(\widetilde{\Omega})$ for $\widetilde{p} > 2$. The isotropic conductivity γ is then recovered from the low frequency CGOs via

$$\gamma(\zeta) = \mathcal{M}(\zeta, 0)^2. \tag{57}$$

As the C^2 isotropic case is well studied in the theoretical and numerical settings, we see that once we obtain the scattering data $\tau(k)$, we can recover the isotropic representation $\gamma(\zeta) = (F_*\sigma)(\zeta)$ of the anisotropic conductivity σ. What remains to be shown now is a way to determine the anisotropic traces of $M_\sigma^\pm$ for $z \in \partial\mathbb{D}$, which we will now do.

3.3. Determining the traces of the anisotropic CGO solutions

Recall, from section 3.2.1, that for fixed $k \in \mathbb{C}$, $W_\sigma^+(z, k)$ denotes the restriction of the anisotropic σ CGO solution $g(z, k)$ of (19) to the exterior domain $\mathbb{C}\backslash\mathbb{D}$, and satisfies (36)–(38)

$$\begin{aligned}
&\overline{\partial}_z W_\sigma^+(z, k) = 0, \quad \text{for } z \in \mathbb{C}\backslash\mathbb{D} \\
&W_\sigma^+(z, k) = e^{ikz}\left(1 + O_k\left(\frac{1}{|z|}\right)\right) \\
&\text{Im}\ \ W_\sigma^+(z, k)\big|_{z\in\partial\mathbb{D}} = \mathcal{H}_\sigma\left(\text{Re}\ \ W_\sigma^+(z, k)\big|_{z\in\partial\mathbb{D}}\right).
\end{aligned}$$

Similarly, for fixed $k \in \mathbb{C}$, $W_\sigma^-(z, k)$ denotes the restriction of the anisotropic $\hat{\sigma}$ CGO solution $\widetilde{g}(z, k)$ of (21) to the exterior domain $z \in \mathbb{C}\backslash\mathbb{D}$, and satisfies (41)–(43)

$$\begin{aligned}
&\overline{\partial}_z W_\sigma^-(z, k) = 0, \quad \text{for } z \in \mathbb{C}\backslash\mathbb{D} \\
&W_\sigma^-(z, k) = e^{ikz}\left(1 + O_k\left(\frac{1}{|z|}\right)\right) \\
&\text{Im}\ \ W_\sigma^-(z, k)\big|_{z\in\partial\mathbb{D}} = \mathcal{H}_{\hat{\sigma}}\left(\text{Re}\ \ W_\sigma^-(z, k)\big|_{z\in\partial\mathbb{D}}\right).
\end{aligned}$$

We will use the boundary relations involving the σ and $\hat{\sigma}$-Hilbert transforms $\mathcal{H}_\sigma$ and $\mathcal{H}_{\hat{\sigma}}$ to derive the BIEs for $M_\sigma^\pm(z, k) = e^{-ikz} W_\sigma^\pm(z, k)$ for $z \in \partial\mathbb{D}$.

Let us first consider the W_σ^+ case. Write $g = W_\sigma^+ = v + iw$ where $v = \text{Re}(W_\sigma^+)$ and $w = \text{Im}(W_\sigma^+)$. Then,

$$\nabla \cdot \sigma \nabla v(z, k) = 0, \qquad \nabla \cdot \hat{\sigma} \nabla w(z, k) = 0.$$

By the definition of $\mathcal{H}_\sigma$ in (24), $\mathcal{H}_\sigma(v|_{\partial\Omega}) = w|_{\partial\Omega}$.

Currently the map $\mathcal{H}_\sigma$ is only defined for real-valued functions. To determine its action on a purely imaginary function now consider $h = -ig = w - iv$. As g satisfies (19) we see that h satisfies

$$\overline{\partial}_z h(z, k) = \mu_1(z)\, \partial_z h(z, k) - \mu_2(z)\, \overline{\partial_z h(z, k)}, \quad z, k \in \mathbb{C},$$

which turns out to be the Beltrami equation corresponding to the anisotropic conductivity $\hat{\sigma}$. Thus $\mathcal{H}_{\hat{\sigma}}(w) = -v$. As $w = \mathcal{H}_{\sigma}(v) = \mathrm{Re}(h)$ it is natural to set

$$\mathcal{H}_{\hat{\sigma}}(w) = i\mathcal{H}_{\sigma}(iw), \tag{58}$$

therefore extending the definition of $\mathcal{H}_{\sigma}$ to all complex-valued functions $g \in H^{1/2}(\partial\Omega)$. Moreover, we have

$$\mathcal{H}_{\sigma} \bigcirc \mathcal{H}_{\hat{\sigma}}(g) = \mathcal{H}_{\hat{\sigma}} \bigcirc \mathcal{H}_{\sigma}(g) = -g + \frac{1}{2\pi}\int_{\partial\mathbb{D}} g \, \mathrm{d}S. \tag{59}$$

For more details (in terms of the isotropic problem), see [66, section 16.3].

If $\sigma = I_{2\times 2}$, then $\mu_1 = 0 = \mu_2$ and the problem reduces to the isotropic $\gamma = 1$ (and $\mu = 0$) case. We briefly review the setting here. The map resulting from $\sigma = I_{2\times 2}$ or equivalently $\gamma = 1$ is $\mathcal{H}_0$, the standard Hilbert transform on the unit circle. $\mathcal{H}_0$ is a singular operator with Fourier multiplier $m(\xi) = -i\xi/|\xi|$ defined for $\xi \in \mathbb{Z}\backslash 0$ with $m(0) = 0$ such that

$$\left\{\mathcal{H}_0 g(\cdot)\right\}^{\wedge}(\xi) = m(\xi)\left\{g(\cdot)\right\}^{\wedge}(\xi) \quad \text{for}\left(g \in \mathrm{L}^2(\partial\mathbb{D})\right).$$

As in [9], we will make use of the projection $\mathcal{P}_0$ of $\mathcal{H}_0$ in the BIEs for the CGOs. The Riesz projection $\mathcal{P}_0$ onto the Hardy spaces on $\partial\mathbb{D}$ is determined by $\mathcal{H}_0$ via

$$\mathcal{P}_0 g = \frac{1}{2}(I + i\mathcal{H}_0)g + \frac{1}{2}\mathcal{L}g, \tag{60}$$

where $\mathcal{L}$ is an averaging operator

$$\mathcal{L}\phi := \left|\partial\Omega\right|^{-1}\int_{\partial\Omega}\phi \, \mathrm{d}S. \tag{61}$$

In the same vain as the isotropic case, we define the projection $\mathcal{P}_{\sigma}$

$$\mathcal{P}_{\sigma} g = \frac{1}{2}(I + i\mathcal{H}_{\sigma})g + \frac{1}{2}\mathcal{L}g, \quad \left(g \in \mathrm{H}^{1/2}\right)(\partial\mathbb{D}). \tag{62}$$

Conjugating with the exponential function yields the k dependent operator defined by

$$\mathcal{P}_{\sigma}^{k}(g)(z) = e^{-ikz}\mathcal{P}_{\sigma}\left(e^{ik\cdot}g\right)(z), \quad \left(g \in \mathrm{H}^{1/2}\right)(\partial\mathbb{D}). \tag{63}$$

Theorem 3.5. *For each fixed $k \in \mathbb{C}$, the boundary traces of the CGO solutions $M_{\sigma}^{\pm}(z, k)$ on $\partial\mathbb{D}$ for the anisotropic σ and $\hat{\sigma}$ Beltrami problems (19) and (21) are the unique solutions to*

$$M_{\sigma}^{+}(z, k) + 1 = \left(\mathcal{P}_0 + \mathcal{P}_{\sigma}^{k}\right)M_{\sigma}^{+}(z, k), \quad z \in \partial\mathbb{D} \tag{64}$$

$$M_{\sigma}^{-}(z, k) + 1 = \left(\mathcal{P}_0 + \mathcal{P}_{\hat{\sigma}}^{k}\right)M_{\sigma}^{-}(z, k), \quad z \in \partial\mathbb{D}. \tag{65}$$

Proof. The σ and $\hat{\sigma}$ proofs are analogous to the isotropic γ and $1/\gamma$ cases with the underlying isotropic Beltrami equation (27) replaced with the their corresponding anisotropic versions (19) and (21), and the Hilbert transform $\mathcal{H}_{\sigma}$ extended to all complex-valued functions $g \in H^{1/2}(\partial\Omega)$ as in (58). See [10] and [66, section 16.3] for more details. □

4. A direct nonlinear D-bar algorithm

The constructive proof described above in section 3 corresponds to a direct nonlinear D-bar algorithm which we summarize here. The reconstruction method from infinite-precision data consists of the following steps:

$$\Lambda_\sigma \xrightarrow{1} M_\sigma^{\pm}(z,k)\big|_{\partial\Omega} \xrightarrow{2} \widetilde{b}_1^{\pm}(k) \xrightarrow{3} \mathbf{t}(k) \xrightarrow{4} \gamma.$$

Step 1: From boundary measurements Λ_σ to traces of the anisotropic CGO solutions $M_\sigma^{\pm}$: for each fixed $k \in \mathbb{C}$, solve the following BIEs for $M_\sigma^{\pm}$

$$M_\sigma^{+}(\,\cdot\,,k)\,\big|_{\partial\Omega} + 1 = \left(\mathcal{P}_\sigma^k + \mathcal{P}_0\right) M_\sigma^{+}(\,\cdot\,,k)\big|_{\partial\Omega}, \tag{66}$$

$$M_\sigma^{-}(\,\cdot\,,k)\,\big|_{\partial\Omega} + 1 = \left(\mathcal{P}_{\hat{\sigma}}^k + \mathcal{P}_0\right) M_\sigma^{-}(\,\cdot\,,k)\big|_{\partial\Omega}, \tag{67}$$

where $\mathcal{P}_\sigma^k$, $\mathcal{P}_{\hat{\sigma}}^k$, and $\mathcal{P}_0$ are the projection operators explained in detail in section 3.3.

Step 2: From the anisotropic CGO traces $M_\sigma^{\pm}$ to the isotropic Beltrami scattering data $\widetilde{b_1^{\pm}}(k)$: substitute the anisotropic traces of $M_\sigma^{\pm}$ into the formula for the nonlinear isotropic Beltrami scattering data

$$\widetilde{b_1^{\pm}}(k) = \frac{1}{2\pi i}\int_{\partial\Omega}\left[M_\sigma^{\pm}(z,k) - 1\right] \mathrm{d}z. \tag{68}$$

Step 3: From Beltrami scattering data $\widetilde{b_1^{\pm}}(k)$ to Schrödinger Scattering data $\mathbf{t}(k)$: for each k, evaluate

$$\mathbf{t}(k) = -4\pi i\bar{k}\ \tau(k), \tag{69}$$

where

$$\tau(k) = \frac{\overline{\widetilde{b}_1^{+}(k)} - \overline{\widetilde{b}_1^{-}(k)}}{2}. \tag{70}$$

Step 4: From the isotropic scattering data to the isotropic conductivity: for each fixed $\zeta \in \widetilde{\Omega}$, solve the $\overline{\partial}_k$-equation

$$\overline{\partial}_k \mathcal{M}(\zeta,k) = \frac{1}{4\pi\bar{k}}\mathbf{t}(k)e(\zeta,-k)\overline{\mathcal{M}(\zeta,k)}, \tag{71}$$

where $\mathcal{M} \sim 1$ for $|\zeta| \to \infty$. The C^2 representative isotropic conductivity is then recovered by $\gamma(\zeta) = \mathcal{M}(\zeta,0)^2$ up to a change of coordinates. Note that as γ is the isotropic representation, we have $\gamma(\zeta) = (F_*\sigma)(\zeta) = \sqrt{\det\left(\sigma\left(F^{-1}(\zeta)\right)\right)}$.

4.1. Numerical setup

In Step 4 of the algorithm, we need to solve the $\overline{\partial}_k$ equation

$$\overline{\partial}_k \mathcal{M}(\zeta, k) = \frac{1}{4\pi\overline{k}} \mathbf{t}(k)\, e(\zeta, -k)\, \overline{\mathcal{M}(\zeta, k)},$$

from Nachman's constructive proof for C^2 isotropic conductivities [68]. To solve the $\overline{\partial}_k$ equation numerically, we need to truncate the scattering data. In [50], it was shown that truncation of the scattering data $\mathbf{t}(k)$ corresponds to a regularization strategy. In this spirit, fix $R > 0$, a positive radius for the k-parameter, and define the truncated scattering transform

$$\mathbf{t}^R(k) = \begin{cases} \mathbf{t}(k) & |k| \leqslant R \\ 0 & |k| > R. \end{cases} \tag{72}$$

To solve the $\overline{\partial}_k$ equation, we use the numerical solution method of Knudsen, Mueller and Siltanen [53], which uses Fourier transforms, and thus we work on the same special k-grid, with $k \in [-R, R]^2$, defined as follows.

Choose $N_k = 2^c$, the number of discretization points in the k_i direction ($i = 1, 2$), for some positive integer c. Set the stepsize in k to be $h_k = \frac{2R}{N_k}$, and form the computational k-grid $\mathcal{G}_c$ by

$$\mathcal{G}_c = \left\{ \mathbf{j} h_k \;\middle|\; \mathbf{j} \in \mathbb{Z}_c^2 \right\}, \tag{73}$$

where

$$\mathbb{Z}_c^2 = \left\{ \mathbf{j} = (j_1, j_2) \in \mathbb{Z} \times \mathbb{Z} \;\middle|\; -2^{c-1} \leqslant j_i < 2^{c-1} \quad i = 1, 2 \right\}. \tag{74}$$

Note that there are $N_k^2 = 2^{2c}$ points in the computational k-grid $\mathcal{G}_c$. Furthermore, the explicit construction in (73)–(74) (which excludes the $j_i = 2^{c-1}$ entries for $i = 1, 2$) is essential for the periodic solution technique used in the solution of the $\overline{\partial}_k$ equation.

We now will describe the numerical implementation of each step of the algorithm.

4.2. Step 1: solving the anisotropic BIEs

The numerical solution of the BIEs (66) and (67) is done by writing the real and imaginary parts separately, replacing all the operators by matrix approximations, and solving the resulting finite linear system. As the BIEs are nearly identical to their isotropic counterparts [9] they can be solved in the same manner as [66, section 16.3]. We review the process here for M_σ^+. The process is analogous for M_σ^-.

We will consider the trigonometric basis functions

$$\phi_n(\theta) = \begin{cases} \pi^{-1/2} \cos\left((n+1)\theta/2\right), & \text{for odd } n, \\ \pi^{-1/2} \sin\left(n\theta/2\right), & \text{for even } n. \end{cases} \tag{75}$$

The D–N map Λ_σ is approximately represented by the matrix $\mathbf{L}_\sigma$ defined by

$$\left(\mathbf{L}_\sigma\right)_{m,n} := \left\langle \Lambda_\sigma \phi_n, \phi_m \right\rangle = \int_{\partial\Omega} \left(\Lambda_\sigma \phi_n\right) \overline{\phi_m}. \tag{76}$$

The tangential derivative map ∂_T can be approximated in the basis (75) by the matrix $\mathbf{D}_T$:

$$\mathbf{D}_T = \begin{bmatrix} 0 & 1 & & & & & \\ -1 & 0 & & & & & \\ & & 0 & 2 & & & \\ & & -2 & 0 & & & \\ & & & & \ddots & & \\ & & & & & 0 & N \\ & & & & & -N & 0 \end{bmatrix}. \tag{77}$$

We approximate $\mathcal{H}_\sigma$ acting on real-valued, zero-mean functions expanded in the basis (75) by

$$\widetilde{\mathbf{H}}_\sigma := \mathbf{D}_T^{-1}\,\mathbf{L}_\sigma. \tag{78}$$

In general, the traces of the CGO solutions at $\partial\mathbb{D}$ do not have mean zero, and so we append the basis function $\phi_0 = (2\pi)^{-1/2}$ to (75). This leads to the following $(2N+1)\times(2N+1)$ matrix approximation to the σ-Hilbert transform $\mathcal{H}_\sigma$:

$$\mathbf{H}_\sigma := \begin{bmatrix} 0_{1\times 1} & 0_{1\times 2N} \\ 0_{2N\times 1} & \widetilde{\mathbf{H}}_\sigma \end{bmatrix}. \tag{79}$$

Furthermore, we can approximate $\mathcal{H}_{\hat{\sigma}}$ when we have $\mathbf{H}_\sigma$ available. We have the identity

$$\mathcal{H}_{\hat{\sigma}} \bigcirc \left(-\mathcal{H}_{\hat{\sigma}}\right) u = \left(-\mathcal{H}_{\hat{\sigma}}\right) \bigcirc \mathcal{H}_\sigma u = u - \mathcal{L}u, \tag{80}$$

so $-\mathcal{H}_{\hat{\sigma}}$ is the inverse operator of $\mathcal{H}_\sigma$ in the subspace of zero-mean functions. Thus we may define a $(2N+1)\times(2N+1)$ matrix approximation to $\mathcal{H}_{\hat{\sigma}}$:

$$\mathbf{H}_{\hat{\sigma}} := \begin{bmatrix} 0_{1\times 1} & 0_{1\times 2N} \\ 0_{2N\times 1} & -\widetilde{\mathbf{H}}_\sigma^{-1} \end{bmatrix}. \tag{81}$$

We represent complex-valued functions $g \in H^{1/2}(\partial\Omega)$ by expanding the real and imaginary parts separately and organizing the transform coefficients as the following vertical vector in $\mathbb{R}^{4N+2}$:

$$\hat{g} = \begin{bmatrix} \left\langle \operatorname{Re} g,\, \phi_0 \right\rangle \\ \left\langle \operatorname{Re} g,\, \phi_1 \right\rangle \\ \vdots \\ \left\langle \operatorname{Re} g,\, \phi_{2N} \right\rangle \\ \left\langle \operatorname{Im} g,\, \phi_0 \right\rangle \\ \left\langle \operatorname{Im} g,\, \phi_1 \right\rangle \\ \vdots \\ \left\langle \operatorname{Im} g,\, \phi_{2N} \right\rangle \end{bmatrix} \in \mathbb{R}^{4N+2}.$$

Denote the direct and inverse transform by $\hat{g} = \widetilde{\mathcal{F}} g$ and $g = \widetilde{\mathcal{F}}^{-1}\hat{g}$. Note that the $(4N+2)\times(4N+2)$ matrix representation of the averaging operator $\mathcal{L}$ is given by

$$\mathbf{L} = \frac{1}{\sqrt{2\pi}} \operatorname{diag}\left[1,\, 0, \ldots, 0,\, 1,\, 0, \ldots, 0\right],$$

where the ones are located at elements $(1,\,1)$ and $(2N+2,\,2N+2)$.

Now we can solve the BIE (66) approximately by solving the following equation for the transform coefficients of M_σ^+:

$$\left(I - \mathbf{P}_\sigma^k - \mathbf{P}_0\right)\widehat{M}_\sigma^+(\ \cdot\ , k)\Big|_{\partial\mathbb{D}} = -\widetilde{\mathcal{F}}(1). \tag{82}$$

Here $\mathbf{P}_\sigma^k$ and $\mathbf{P}_0$ stand for approximate implementations of the actions of the operators $\mathcal{P}_\sigma^k$ and $\mathcal{P}_0$, respectively. The action of $\mathcal{P}_\sigma$ (defined in (62)) in the transform domain is

$$\mathbf{P}_\sigma\,\widehat{g} = \frac{1}{2}\left(I + i\begin{bmatrix}\mathbf{H}_\sigma & 0\\ 0 & \mathbf{H}_{\hat{\sigma}}\end{bmatrix}\right)\widehat{g} + \frac{1}{2}\mathbf{L}\,\widehat{g},$$

where $\mathbf{H}_\sigma$ and $\mathbf{H}_{\hat{\sigma}}$ are given by (79) and (81), respectively. The action of $\mathcal{P}_\sigma^k$ (defined in (63)) in the transform domain is

$$\mathbf{P}_\sigma^k\,\widehat{g} = \widetilde{\mathcal{F}}\left(e^{-ikz}\cdot\widetilde{\mathcal{F}}^{-1}\left(\mathbf{P}_\sigma\,\widetilde{\mathcal{F}}\left(e^{ikz}\cdot\left(\widetilde{\mathcal{F}}^{-1}\widehat{g}\right)\right)\right)\right). \tag{83}$$

Now one can solve equation (82) for the transform coefficients $\widehat{M}_\sigma^+$ iteratively using GMRES.

4.3. Step 2: computing the Beltrami scattering data

For the given value $k \in \mathbb{C}$, we compute $\widetilde{b}_1^{\pm}(k)$ from (68)

$$\widetilde{b}_1^{\pm}(k) = \frac{1}{2\pi i}\int_{\partial\Omega}\left[M_\sigma^{\pm}(z, k) - 1\right]\mathrm{d}z.$$

Letting $z = e^{i\theta} \in \partial\mathbb{D}$, $\theta \in [0, 2\pi)$ we have $\mathrm{d}z = ie^{i\theta}\mathrm{d}\theta$ and

$$\widetilde{b}_1^{\pm}(k) = \frac{1}{2\pi}\int_0^{2\pi}\left[M_\sigma^{\pm}\left(e^{i\theta}, k\right) - 1\right]e^{i\theta}\ \mathrm{d}\theta.$$

We can now approximate the continuous integral above using a finite sum:

$$\widetilde{b_1^{\pm}}(k) \approx \frac{\Delta\theta}{2\pi}\sum_{n=1}^{N_z}\left[M_\sigma^{\pm}\left(e^{i\theta_n}, k\right) - 1\right]e^{i\theta_n}, \tag{84}$$

where $n = 1, \ldots, N_z$ are the indices for the function values $M_\sigma^{\pm}(z_n, k)$ obtained numerically in Step 1 above, and $\Delta\theta$ denotes the stepsize in θ along the unit circle.

4.4. Step 3: computing the Schrödinger scattering data

The isotropic (truncated) Schrödinger scattering data $\mathbf{t}^R(k)$ is then computed by (69)

$$\mathbf{t}^R(k) = \begin{cases} -4\pi i\bar{k}\tau(k) & |k| \leqslant R\\ 0 & |k| > R,\end{cases} \tag{85}$$

where $\tau(k)$ is evaluated via (70)

$$\tau(k) = \frac{\overline{\widetilde{b}_1^{+}(k)} - \overline{\widetilde{b}_1^{-}(k)}}{2}.$$

4.5. Step 4: solving the D-bar equation

As $\mathcal{M} \sim 1$ for $|\zeta| \to \infty$, and $\frac{1}{\pi k}$ is the fundamental solution for the $\overline{\partial}_k$ operator, the solution to the $\overline{\partial}_k$ equation

$$\overline{\partial}_k \mathcal{M}(\zeta, k) = \frac{1}{4\pi\overline{k}} \mathbf{t}(k)\, e(\zeta, -k)\, \overline{\mathcal{M}(\zeta, k)},$$

can be written as

$$\mathcal{M}(\zeta, k) = 1 + \frac{1}{\pi} \int_{\mathbb{R}^2} \frac{\mathbf{t}(\kappa)\, e(\zeta, -\kappa)\, \overline{\mathcal{M}(\zeta, \kappa)}}{4\pi\overline{\kappa}\,(k - \kappa)}\, \mathrm{d}\kappa_1 \mathrm{d}\kappa_2, \tag{86}$$

or in terms of convolutions

$$\mathcal{M}(\zeta, k) = 1 + \frac{1}{\pi k} * \left(\frac{1}{4\pi\overline{k}} \mathbf{t}(k)\, e(\zeta, -k)\, \overline{\mathcal{M}(\zeta, k)} \right), \tag{87}$$

where the convolution takes place in the k variable. Note that the integration takes place over the entire plane. Using the truncated scattering data $\mathbf{t}^R$ we can instead find the regularized solution $\mathcal{M}_R(\zeta, k)$ by solving

$$\mathcal{M}_R(\zeta, k) = 1 + \frac{1}{\pi} \int_{|\kappa| \leqslant R} \frac{\mathbf{t}^R(\kappa)\, e(\zeta, -\kappa)\, \overline{\mathcal{M}_R(\zeta, \kappa)}}{4\pi\overline{\kappa}\,(k - \kappa)}\, \mathrm{d}\kappa_1 \mathrm{d}\kappa_2, \tag{88}$$

or in terms of convolutions

$$\mathcal{M}_R(\zeta, k) = 1 + \frac{1}{\pi k} * \left(\frac{1}{4\pi\overline{k}} \mathbf{t}^R(k)\, e(\zeta, -k)\, \overline{\mathcal{M}_R(\zeta, k)} \right), \tag{89}$$

where the integration now takes place over a disc of radius R.

From [50, 65] this gives the correct result as $R \to \infty$. To solve for $\mathcal{M}_R$ numerically, we exploit the convolution using Fourier transforms and Vainikko's fast solution method on the special k-grid defined above in section 4.1 by

$$\begin{aligned} \mathcal{M}_R(\zeta, k) &= 1 + \mathcal{F}^{-1}\left\{ \mathcal{F}\left(\frac{1}{\pi k} * \frac{1}{4\pi\overline{k}} \mathbf{t}^R(k)\, e(\zeta, -k)\, \overline{\mathcal{M}_R(\zeta, k)} \right) \right\} \\ &= 1 + \mathcal{F}^{-1}\left\{ \mathcal{F}\left(\frac{1}{\pi k} \right) \mathcal{F}\left(\frac{1}{4\pi\overline{k}} \mathbf{t}^R(k)\, e(\zeta, -k)\, \overline{\mathcal{M}_R(\zeta, k)} \right) \right\}. \end{aligned} \tag{90}$$

The singularity at $k = 0$ is dealt with in the following way. The $k = 0$ entry for $\mathbf{t}^R(k)/\overline{k}$ is set to zero, its analytic limiting value. Additionally, the fundamental solution $\frac{1}{\pi k}$ is set to zero for $k = 0$ (see [52] for further details). The resulting system in (90) can then be solved using matrix-free GMRES.

After solving (90) for a given $\zeta \in \widetilde{\Omega}$, the $k = 0$ entry $\mathcal{M}_R(\zeta, 0)$ is saved. This step is repeated (in parallel if desired) for each $\zeta \in \widetilde{\Omega}$. The isotropic (regularized) C^2 conductivity γ_R is then determined by

$$\gamma_R(\zeta) = \left(\mathcal{M}_R(\zeta, 0) \right)^2 \approx \sqrt{\det\left(\sigma\left(F^{-1}(\zeta) \right) \right)}. \tag{91}$$

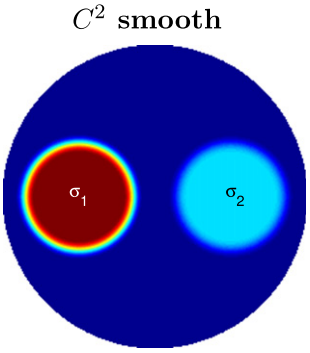

Figure 2. The C^2 smooth two circular inclusions phantom used in Test 1. The conductivities in the left circular region, σ_1, and in the right circular region, σ_2, are defined in (92). The background conductivity is the 2×2 identity matrix.

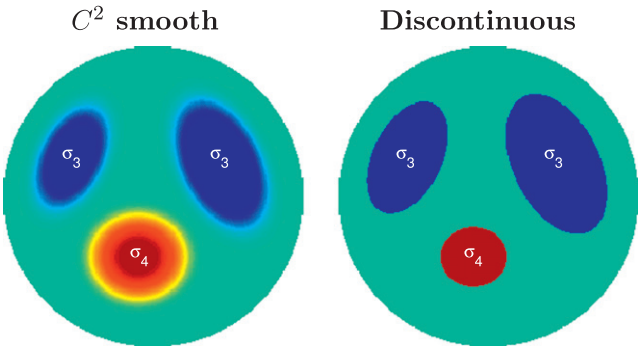

Figure 3. The heart and lungs phantom used in Test 2. The C^2 smooth and corresponding piecewise constant phantoms are shown on the left and right, respectively. The conductivity in the oval lungs regions, σ_3, and in the circular heart region, σ_4, are defined in (93). The background conductivity is the 2×2 identity matrix.

5. Numerical results and discussion

We tested the algorithm presented in section 4 on simulated anisotropic EIT data for both C^2 smooth conductivities and piecewise-constant conductivities (see figures 2 and 3). For each phantom, we solved the anisotropic conductivity equation (3)

$$\nabla \cdot \sigma \nabla u = 0,$$

with Neumann boundary condition $\sigma \frac{\partial u}{\partial \nu} = \phi_j$ on $\partial\Omega$defined by (75), for $j = 1, \ldots 32$, using the finite element method (FEM). The numerical FEM solution was used to form a 33×33 discrete matrix approximation $\mathbf{R}_\sigma$ to the Neumann-to-Dirichlet map, and subsequently the discrete matrix approximation $\mathbf{L}_\sigma$ to the D–N map Λ_σ as described in [66].

The traces of the anisotropic CGO solutions $M_\sigma^{\pm}$ were solved numerically (via (82), for $z = e^{i\theta} \in \partial\Omega$ where

$$\theta \in \frac{2\pi}{33}\big[-16, -15, \ldots, -1, 0, 1, \ldots, 15, 16\big].$$

The scattering radius R and corresponding k-grid are specific to each problem and are stated below. In each example, the $\overline{\partial}_k$ equation (71) was solved for $|\zeta| \leqslant 1.2$ with step-size $h_\zeta = 0.0094$, where the truncated isotropic representative conductivity $\gamma_R(\zeta) \approx (F_*\sigma)(\zeta) = \sqrt{\det \sigma\,(F^{-1}(\zeta))}$ was recovered.

Our FEM computations were performed using MATLAB's PDE toolbox. The basis functions were piecewise linear, and the triangular mesh generated for the unit disc domain comprised of 262 144 triangles and 131 585 vertices. The conductivity values were specified at the barycenter of each triangle. Thus, strictly speaking, none of our computational conductivity models were really C^2 but rather piecewise constant in a relatively fine triangular tiling, and the conductivity function used to specify the values of the coefficient σ was C^2 smooth. A more detailed analysis of the effect of piecewise constant approximations is outside the scope of this paper.

Without parallelization, the algorithm takes approximately 5 s on a standard laptop when using a 32×32 scattering k-grid and reconstructing on a 32×32 spatial ζ-grid. The reconstructions shown here were computed using a 128×128 scattering grid and 256×256 spatial grid, to show higher resolution, and took approximately 45 min each (again, without parallelization). We note that the algorithm is parallelizable in the following steps: $\Lambda_\sigma \longrightarrow \mathbf{t}(k)$ (in k), and $\mathbf{t}(k) \longrightarrow \gamma_R(\zeta)$ (in ζ). A detailed study of optimizing the algorithm for faster reconstructions is outside the scope of this paper.

5.1. Test 1: two circular inclusions

Our first test involves the C^2 smooth anisotropic phantom shown in figure 2 with two circular inclusions with orthogonal directional preferences

$$\sigma_1 = \begin{bmatrix} 1 & 0 \\ 0 & 4 \end{bmatrix}, \qquad \sigma_2 = \begin{bmatrix} 2 & 0 \\ 0 & 1 \end{bmatrix}. \tag{92}$$

The right inclusion is more conductive in the vertical direction whereas the left inclusion more conductive in the horizontal direction.

The BIE (82) was solved to recover $M_\sigma^\pm$ for $z \in \partial\mathbb{D}$ as described above, with $|k| \leqslant 6$ to evaluate the scattering transform $\mathbf{t}_R(k)$ on a k-grid with a step-size of $h_k \approx 0.094$. The $\overline{\partial}_k$-equation was then solved, and the truncated isotropic representative conductivity $\gamma_R(\zeta) \approx (F_*\sigma)(\zeta) = \sqrt{\det \sigma\,(F^{-1}(\zeta))}$ was recovered. Figure 3 shows the reconstructed isotropization $\gamma_R(\zeta)$ (right) and the true $\sqrt{\det \sigma\,(\zeta)}$ (middle) in the deformed coordinates, as well as the true $\sqrt{\det \sigma\,(z)}$ in the physical coordinates. In $\sqrt{\det \sigma}$, the prescribed maximum value of the left inclusion is 2, and 1.41 in the right inclusion. The reconstructed maximums are 2.34 and 1.61, respectively.

The anisotropy is visible in the isotropic representation γ_R through the coordinate deformation (circles squeezed into ellipses). This is due to the precise underlying quasiconformal map F which satisfies

$$\sqrt{\det \sigma}\begin{pmatrix} 1 & 0 \\ 0 & 1 \end{pmatrix} = \frac{1}{J_F}\, DF\ \sigma\,(DF)^t$$

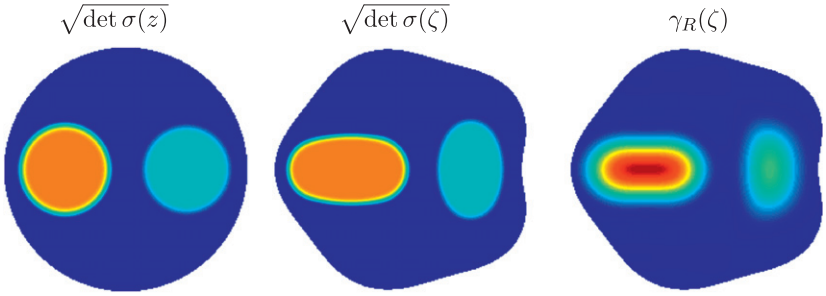

Figure 4. Results for the C^2 smooth circular inclusions phantom of figure 2 in Test 1. Left: isotropization of the true conductivity σ shown in the physical coordinates. Middle: isotropization of the true conductivity σ shown in the deformed coordinates. Right: reconstruction of the isotropization of σ in the deformed coordinates. The scattering transform $\mathbf{t}_R(k)$ was computed for $|k| \leqslant 6$. The values of the reconstruction γ_R are very similar to the true values (left and middle), and the change of coordinates is evident from the squeezed ellipses. The figures are plotted on the same color scale for ease of comparison.

where DF denotes the Jacobian of the map F, J_F the determinant of the Jacobian DF, and t the transpose. For z inside the inclusion $\sigma_1(z) = \left(\begin{smallmatrix} 1 & 0 \\ 0 & 4 \end{smallmatrix}\right)$ the map will deform the coordinates (approximately) by F: $z = (x, y) \mapsto (x, \frac{1}{2}y)$. Similarly for $z \in \sigma_2(z) = \left(\begin{smallmatrix} 2 & 0 \\ 0 & 1 \end{smallmatrix}\right)$, the map will behave (approximately) as F: $z = (x, y) \mapsto (\frac{1}{\sqrt{2}}x, y)$ which provides intuition for the vertical and horizontal squeezing displayed in the reconstructions of figure 5.

5.2. Test 2: a heart and lungs phantom

Our next test involves the anisotropic phantoms shown in figure 3 with two oval inclusions (lungs) and a circular inclusion (heart) with conductive directional preferences

$$\sigma_3 = \begin{bmatrix} 0.4 & 0 \\ 0 & 0.8 \end{bmatrix}, \qquad \sigma_4 = \begin{bmatrix} 6 & 0 \\ 0 & 2 \end{bmatrix}. \tag{93}$$

The ovular lung inclusions are less conductive than the background with a directional preference in the x_2 direction whereas the heart shaped inclusion more conductive in the x_1 direction. Here we consider a piecewise constant phantom and its C^2 smoothed version (right and left in figure 3, respectively). Clearly this is an idealized version of a 2D cross-section and does not model the true 3D nature of the anistropy present in the heart.

We first work with the C^2 smoothed phantom shown in figure 4. The BIE (82) was solved to recover $M_\sigma^\pm$ for $z \in \partial\mathbb{D}$ as described above, with $|k| \leqslant 7$ to evaluate the scattering transform $\mathbf{t}_R(k)$ on a k-grid with a stepsize of $h_k \approx 0.109$. The $\overline{\partial}_k$-equation was then solved and the isotropic representative conductivity $\gamma_R(\zeta) \approx (F_*\sigma)(\zeta) = \sqrt{\det \sigma\,(F^{-1}(\zeta))}$ was recovered. figure 5 shows the reconstructed $\gamma_R(\zeta)$ along with $\sqrt{\det \sigma\,(\zeta)}$. The maximum value in $\sqrt{\det \sigma}$ occurs in the *heart* with a value of 3.46 and the minimum in the *lungs* with a value of 0.57. The recovered values are 4.42 and 0.50, respectively. The change of coordinates is evident as the lungs are squeezed vertically and the heart horizontally.

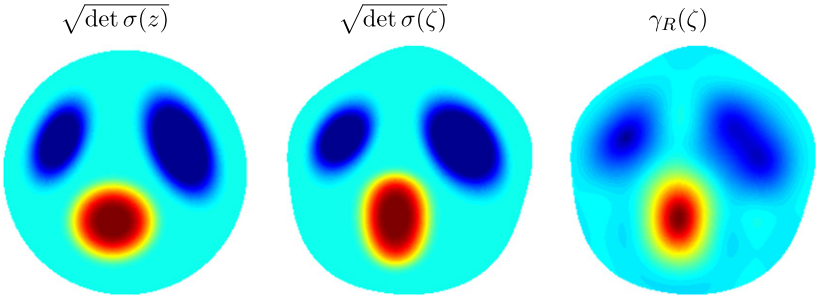

Figure 5. Results for the C^2 smooth heart and lungs phantom in figure 3 in Test 2. Left: isotropization of the true conductivity σ shown in the physical coordinates. Middle: isotropization of the true conductivity σ shown in the deformed coordinates. Right: reconstruction of the isotropization of σ in the deformed coordinates. The scattering transform $\mathbf{t}_R(k)$ was computed for $|k| \leqslant 7$. The squeezing in the isotropic reconstruction γ_R clearly shows stronger x_1 and x_2 anisotropies in the heart and lung inclusions, respectively. The figures are plotted on the same color scale for ease of comparison.

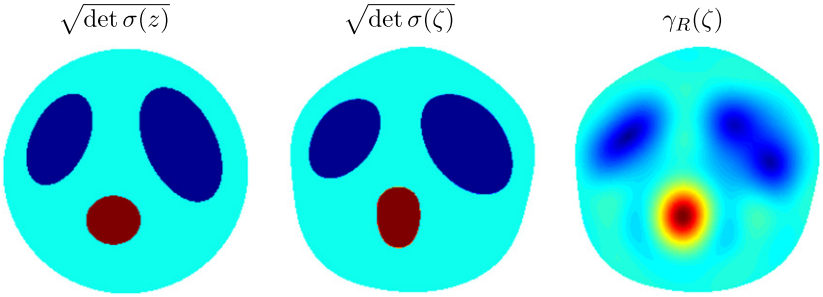

Figure 6. Results for the piecewise constant heart and lungs phantom in figure 3 in Test 2. Left: isotropization of the true conductivity σ shown in the physical coordinates. Middle: isotropization of the true conductivity σ shown in the deformed coordinates. Right: reconstruction of the isotropization of σ in the deformed coordinates. The scattering transform $\mathbf{t}_R(k)$ was computed for $|k| \leqslant 7$. Again, the squeezing in the isotropic reconstruction γ_R clearly shows stronger x_1 and x_2 anisotropies in the heart and lung inclusions, respectively. The figures are plotted on the same color scale for ease of comparison.

It should be noted that while the theory described above does not theoretically hold for discontinuous phantoms, as we passed to the C^2 smooth proof of Nachman [68], the D-bar algorithm resulting from Nachman's Schrödinger based C^2 proof has been used effectively on piecewise constant phantoms suggesting that the Schrödinger based D-bar algorithm can be used on discontinuous phantoms. In light of this, we tested the algorithm on the discontinuous version of the C^2 phantom also shown in figure 3.

The same k and z grids were used as in the C^2 smoothed case. figure 6 shows the reconstructed γ_R again with strong x_1 anisotropy in the heart and x_2 in the lungs clearly visible via the squeezing of the underlying change of coordinates. Here the maximum and minimum recovered values are are 4.03 and 0.47, respectively.

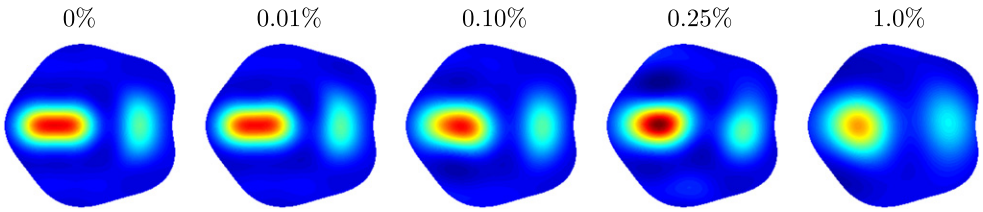

Figure 7. Reconstructions of the C^2 smooth circular inclusions phantom of figure 2 in Test 1 with various levels of additional noise added to the voltage data. The scattering data for the reconstructions, from left to right, were computed for $|k| \leqslant 6.0$, 5.9, 5.0, 4.8 and 3.8. The figures are plotted on the same color scale for ease of comparison. Notice that as the level of noise increases, the approximate values of the associated isotropic conductivity $\sqrt{\det \sigma}$ are retained, however the directional preferences of the underlying anisotropy become less pronounced.

Table 1. Maximum values in the reconstructed isotropizations shown in figure 7.

Noise level	True	0%	0.01%	0.10%	0.25%	1.0%
Left inclusion	2.00	2.34	2.31	2.32	2.54	2.05
Right inclusion	1.41	1.61	1.60	1.61	1.55	1.45

5.3. Test 3: increased noise

We now revisit the C^2-smooth phantom in Test 1, and introduce Gaussian relative noise to the simulated FEM voltage data as follows. Let V^j denote the vector of computed boundary voltages for the jth current pattern, η the noise level, and N^j a Gaussian random vector (generated by the `randn` command in MATLAB) that is unique for each current pattern j. Denote by $\widetilde{V}^j$ the noisy voltage data computed by

$$\widetilde{V}^j = V^j + \eta N^j \max \left| V^j \right|, \quad 1 \leqslant j \leqslant 32.$$

The corresponding noisy N–D matrix $\widetilde{\mathbf{R}}_\sigma$ was then computed using $\widetilde{R}_\sigma \phi_j = \widetilde{V}^j$. The noisy D–N matrix $\widetilde{L}_\sigma$ was then formed using $\widetilde{\mathbf{R}}_\sigma$.

Figure 7 shows the reconstructions with 0%, 0.01%, 0.10%, 0.25%, and 1.0% Gaussian relative noise added to the voltage data. As the level of noise increased, the radius for the scattering data was forced to decrease, i.e. from $|k| \leqslant 6.0$, 5.9, 5.0, 4.8, and 3.8. table 1 contains the maximum values of the left and right inclusions in the reconstructions for the various levels of noise. It is clear that as the noise level increases it is still possible to determine the approximate values for the isotropic representative conductivity $\sqrt{\det \sigma}$, although the directional preference of the underlying anisotropy becomes less pronounced. A more detailed study of various types of additional noise is outside the scope of this paper, see [38] for a discussion of how noise levels are specific to the EIT device.

5.4. The deformed boundary

It should be noted that the representative isotropic conductivities γ_R displayed in this paper are shown on their true deformed boundary (calculated by solving (12) for each known

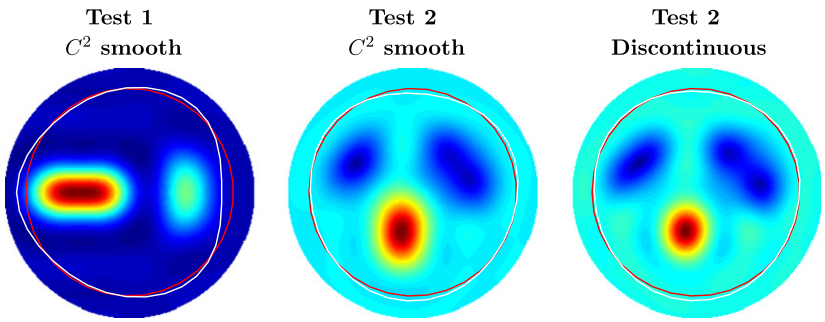

Figure 8. Reconstructions of Tests 1 and 2 for $|\zeta| < 1.2$. The red line indicates the unit circle, the original boundary $\partial\mathbb{D}$, whereas the white line represents the deformed boundary calculated via (12). Notice that the deformation is clearly contained inside the larger domain.

anisotropic σ). In practice, this information is not readily available. However, figure 8 shows the deformations of the examples, from Tests 1 and 2, compared to the original boundary ($\partial\,\mathbb{D}$) and a circle of radius 1.2. Notice that the deformation is clearly contained inside the disc of radius 1.2, suggesting that recovering the anisotropic conductivity on a slightly larger domain is sufficient to contain the interior behavior. Furthermore, as the D-bar method used here allows for point-wise reconstructions for a given point ζ and it is known that $\gamma \equiv 1$ outside $\widetilde{\Omega}$, one can merely compute at additional ζ points outside of the original domain $\Omega = \mathbb{D}$ to ensure that the deformed domain is in fact contained. The reconstruction γ_R should be interpreted as a reconstruction in isothermal coordinates, similar to sonograms in ultrasound imaging.

We remind the reader that alternatively one could attempt to construct the precise deformation of the boundary $F(\partial\mathbb{D}) = \partial\widetilde{\Omega}$. However, this requires the construction of the highly unstable map F [6] via a high-frequency k limit of the CGO solutions (54), for $z \in \partial\,\mathbb{D}$

$$F(z) = \lim_{|k|\to\infty} \frac{\log W_\sigma^+(z, k)}{ik}, \qquad z \in \mathbb{C}\backslash\mathbb{D},$$

where the logarithm is not necessarily taken with respect to the principal branch. The traces of the CGO solutions $W_\sigma^+(z, k)$ are highly unstable for large k making such a limit impractical numerically. An in-depth analysis of the stability of such an endeavor is outside the scope of this paper.

6. Conclusions

In this paper, we have presented a constructive CGO based D-bar proof for C^2 smooth anisotropic conductivities in the plane which does not require the construction of the unstable *push-forward* map F used previously in the L^∞ proof of [6], and previous CGO based 2D anisotropic proofs. The new proof, presented here, results in the first noise-robust nonlinear D-bar algorithm for the anisotropic conductivity problem in 2D EIT. We have demonstrated that the numerical D-bar algorithm performs well on simulated anisotropic EIT data and noise-robust images of isotropic, or scalar-valued, conductivities that are distorted versions of the original anisotropic conductivities, can be reliably recovered.

We emphasize that non-uniqueness of the anisotropic inverse conductivity problem should not be such a game-ender and remind the reader that even the isotropic inverse conductivity problem is so severely ill-posed that strong regularization is needed for robust image formation from noisy data. In a similar fashion to linear inverse problems, non-uniqueness can be dealt with by picking out a unique representative from the same-data equivalence class, which can still provide useful information. In addition, when the proposed method is applied to isotropic data, the result coincides with the traditional isotropic D-bar method.

The results of this paper additionally help to explain the geometric distortion observed in isotropic D-bar imaging when there is insufficient knowledge of the boundary, or when the underlying conductivity is in fact anisotropic. Furthermore, the approach used here paves the way for direct regularized EIT for matrix-valued conductivities, one of the most important aspects of any practical inverse problem, and essential for ensuring a noise-robust reconstruction algorithm.

Acknowledgments

This study was supported by the SalWe Research Program for Mind and Body (Tekes—the Finnish Funding Agency for Technology and Innovation grant 1104/10) and by the Academy of Finland (*Finnish Centre of Excellence in Inverse Problems Research* 2012-2017, decision number 250215).

References

[1] Abascal J-F P, Arridge S R, Atkinson D, Horesh R, Fabrizi L, Lucia M D, Horesh L, Bayford R H and Holder D S 2003 Use of anisotropic modelling in electrical impedance tomography; description of method and preliminary assessment of utility in imaging brain function in the adult human head *Neuroimage* **8** 258–68

[2] Abascal J-F P, Arridge S R, Lionheart W R, Bayford R H and Holder D S 2007 Validation of a finite-element solution for electrical impedance tomography in an anisotropic medium *Physiol. Meas.* **28** S129–40

[3] Abubakar A, Habashy T M, Li M and Liu J 2009 Inversion algorithms for large-scale geophysical electromagnetic measurements *Inverse Probl.* **25** 123012

[4] Arwadi T E 2012 Error estimates for reconstructed conductivities via the D-bar method *Numer. Funct. Anal. Optim.* **33** 719–35

[5] Astala K, Iwaniec T and Martin G 2009 *Elliptic Partial Differential Equations and Quasiconformal Mappings in the Plane* (*Mathematical Series* vol 48) (Princeton, NJ: Princeton University Press)

[6] Astala K, Lassas M and Päivärinta L 2005 Calderón's inverse problem for anisotropic conductivity in the plane *Comm. Part. Diff. Eqns* **30** 207–24

[7] Astala K, Mueller J, Päivärinta L, Perämäki A and Siltanen S 2011 Direct electrical impedance tomography for nonsmooth conductivities *Inverse Probl. Imaging* **5** 531–49

[8] Astala K, Mueller J, Päivärinta L and Siltanen S 2010 Numerical computation of complex geometrical optics solutions to the conductivity equation *Appl. Comput. Harmon. Anal.* **29** 391–403

[9] Astala K and Päivärinta L 2006 A boundary integral equation for Calderón's inverse conductivity problem *Proc. 7th Int. Conf. on Harmonic Analysis, Collectanea Mathematica*

[10] Astala K and Päivärinta L 2006 Calderón's inverse conductivity problem in the plane *Ann. Math.* **163** 265–99

[11] Astala K, Päivärinta L, Reyes J M and Siltanen S 2013 Nonlinear Fourier analysis for discontinuous conductivities: computational results Submitted manuscript arXiv:1310.7051v1

[12] Barber D C and Brown B H 1990 Progress in electrical impedance tomography *Inverse Problems in Partial Differential Equations (Arcata, CA, 1989)* (Philadelphia, PA: SIAM) pp 151–64

[13] Barceló J A, Barceló T and Ruiz A 2001 Stability of the inverse conductivity problem in the plane for less regular conductivities *J. Diff. Eqns* **173** 231–70
[14] Barceló T, Faraco D and Ruiz A 2007 Stability of Calderón inverse conductivity problem in the plane *J. Math. Pure Appl.* **88** 522–56
[15] Beals R and Coifman R R 1985 Multidimensional inverse scatterings and nonlinear partial differential equations *Pseudodifferential Operators and Applications (Notre Dame, IN, 1984)* (Providence, RI: Ameican Mathematical Society) pp 45–70
[16] Bikowski J 2008 Electrical impedance tomography reconstructions in two and three dimensions; from Calderón to direct methods *PhD Thesis* Colorado State University, Fort Collins, CO
[17] Bikowski J, Knudsen K and Mueller J L 2011 Direct numerical reconstruction of conductivities in three dimensions using scattering transforms *Inverse Problems* **27** 19
[18] Blåsten E 2013 On the Gelfand-Calderón inverse problem in two-dimensions, *PhD Thesis* University of Helsinki, Finland
[19] Breckon W R 1992 The problem of anisotropy in electrical impedance tomography *Proc. 14th Int. Conf. of the IEEE Engineering in Medicine and Biology Society (Paris)* **5** 1734–35
[20] Brown R M and Uhlmann G 1997 Uniqueness in the inverse conductivity problem for nonsmooth conductivities in two dimensions *Commun. Part. Diff. Eqns* **22** 1009–27
[21] Bukhgeim A 2008 Recovering the potential from Cauchy data in two dimensions *J. Inverse III-Posed Probl.* **16** 19–34
[22] Calderón A-P 1980 On an inverse boundary value problem *Seminar on Numerical Analysis and its Applications to Continuum Physics (Rio de Janeiro, 1980)* (Rio de Janeiro: Soc. Brasil. Mat.) pp 65–73
[23] Clop A, Faraco D and Ruiz A 2010 Integral stability of Calderón inverse conductivity problem in the plane *Inverse Probl. Imaging* **4** 49–91
[24] Costa E, Lima R and Amato M 2009 Electrical impedance tomography *Curr. Opin. Crit. Care* **15** 18–24
[25] Dardé J, Hyvönen N, Seppänen A and Staboulis S 2013 Simultaneous reconstruction of outer boundary shape and admittivity distribution in electrical impedance tomography *SIAM J. Imaging Sci.* **6** 176–98
[26] Dardé J, Hyvönen N, Seppänen A and Staboulis S 2013 Simultaneous recovery of admittivity and body shape in electrical impedance tomography: an experimental evaluation *Inverse Problems* **29** 085004
[27] DeAngelo M and Mueller J L 2010 2D D-bar reconstructions of human chest and tank data using an improved approximation to the scattering transform *Physiol. Meas.* **31** 221–32
[28] Delbary F, Hansen P C and Knudsen K 2012 Electrical impedance tomography: 3D reconstructions using scattering transforms *Appl. Anal.* **91** 737–55
[29] Engl H, Hanke M and Neubauer A 1996 Regularization of inverse problems *Mathematics and Its Applications* (Berlin: Springer)
[30] Faddeev L D 1966 Increasing solutions of the Schrödinger equation *Sov. Phys. Dokl.* **10** 1033–5
[31] Francini E 2000 Recovering a complex coefficient in a planar domain from Dirichlet-to-Neumann map *Inverse Problems* **16** 107–19
[32] Frerichs I 2000 Electrical impedance tomography (EIT) in applications related to lung and ventilation: a review of experimental and clinical activities *Physiol. Meas.* **21** 1–21
[33] Glidewell M E and Ng K T 1995 Anatomically constrained electrical impedance tomography for anisotropic bodies via a two-step approach *IEEE Trans. Med. Imaging* **14** 498–503
[34] Glidewell M E and Ng K T 1997 Anatomically constrained electrical impedance tomography for three-dimensional anisotropic bodies *IEEE Trans. Med. Imaging* **16** 572–80
[35] Greenleaf A, Lassas M and Uhlmann G 2003 Anisotropic conductivities that cannot be detected by EIT *Physiol. Meas.* **24** 413
[36] Greenleaf A, Lassas M and Uhlmann G 2003 On nonuniqueness for Calderón's inverse problem *Math. Res. Lett.* **10** 685–94
[37] Hamilton S, Herrera C, Mueller J L and VonHerrmann A 2012 A direct D-bar reconstruction algorithm for recovering a complex conductivity in 2D *Inverse Problems* **28** 095005
[38] Hamilton S J and Mueller J L 2013 Direct EIT reconstructions of complex admittivities on a chest-shaped domain in 2D *IEEE Trans. Med. Imaging* **32** 757–69
[39] Henkin G and Santacesaria M 2010 On an inverse problem for anisotropic conductivity in the plane *Inverse Problems* **26** 095011

[40] Herrera C N L 2012 Um metodo D-bar para estimar admitividade em 2D atraves de tomografia por impedancia electrica *PhD Thesis* University of São Paulo, São Paulo, Brazil
[41] Holder D (ed) 2005 *Electrical Impedance Tomography; Methods, History, and Applications* (Bristol: Institute of Physics Publishing)
[42] Isaacson D, Mueller J, Newell J and Siltanen S 2006 Imaging cardiac activity by the D-bar method for electrical impedance tomography *Physiol. Meas.* **27** 43–50
[43] Isaacson D, Mueller J L, Newell J C and Siltanen S 2004 Reconstructions of chest phantoms by the D-bar method for electrical impedance tomography *IEEE Trans. Med. Imaging* **23** 821–8
[44] Iwaniec T and Martin G 2001 *Geometric Function Theory and Non-linear Analysis* (*Oxford Mathematical Monographs*) (Oxford: Oxford University Press)
[45] Kang H and Yun K 2003 Boundary determination of conductivities and Riemannian metrics via local Dirichlet-to-Neumann operator *SIAM J. Math. Anal.* **34** 719–35
[46] Kao T-J, Boverman G, Kim B S, Isaacson D, Saulnier G, Newell J, Choi M, Moore R and Kopans D 2008 Regional admittivity spectra with tomosynthesis images for breast cancer detection: preliminary patient study *IEEE Trans. Med. Imaging* **27** 1762–8
[47] Kao T-J, Saulnier G, Xia H, Tamma C, Newell J and Isaacson D 2007 A compensated radiolucent electrode array for combined EIT and mammography *Physiol. Meas.* **28** S291
[48] Kim B, Isaacson D, Xia H, Kao T, Newell J and Saulnier G 2007 A method for analyzing electrical impedance spectroscopy data from breast cancer patients *Physiol. Meas.* **28** S237–46
[49] Knudsen K 2003 A new direct method for reconstructing isotropic conductivities in the plane *Physiol. Meas.* **24** 391–403
[50] Knudsen K, Lassas M, Mueller J and Siltanen S 2009 Regularized D-bar method for the inverse conductivity problem *Inverse Probl. Imaging* **3** 599–624
[51] Knudsen K and Mueller J L 2011 The Born approximation and Calderón's method for reconstructions of conductivities in 3-D *Discret. Contin. Dyn. Syst.* **2011** 884–93
[52] Knudsen K, Mueller J and Siltanen S 2004 Numerical solution method for the dbar-equation in the plane *J. Comput. Phys.* **198** 500–17
[53] Knudsen K and Tamasan A 2004 Reconstruction of less regular conductivities in the plane *Commun. Part. Diff. Eqns* **29** 361–81
[54] Kohn R and Vogelius M 1984 Determining conductivity by boundary measurements *Commun. Pure Appl. Math.* **37** 289–98
[55] Kohn R V and Vogelius M 1985 Determining conductivity by boundary measurements II. Interior results *Commun. Pure Appl. Math.* **38** 643–67
[56] Kolehmainen V, Lassas M and Ola P 2005 The inverse conductivity problem with an imperfectly known boundary *SIAM J. Appl. Math.* **66** 365–83
[57] Kolehmainen V, Lassas M and Ola P 2008 Electrical impedance tomography problem with inaccurately known boundary and contact impedances *IEEE Trans. Med. Imaging* **27** 1404–14
[58] Kolehmainen V, Lassas M and Ola P 2010 Calderón's inverse problem with an imperfectly known boundary and reconstruction up to a conformal deformation *SIAM J. Math. Anal* **42** 1371–81
[59] Kolehmainen V, Lassas M, Ola P and Siltanen S 2013 Recovering boundary shape and conductivity in electrical impedance tomography *Inverse Probl. Imaging* **7** 217–42
[60] Lassas M, Taylor M and Uhlmann G 2003 The Dirichlet-to-Neumann map for complete Riemannian manifolds with boundary *Commun. Anal. Geom.* **11** 207–22
[61] Lassas M and Uhlmann G 2001 On determining a Riemannian manifold from the Dirichlet-to-Neumann map *Ann. Sci. École Norm. Sup.* **4** 771–87
[62] Lee J and Uhlmann G 1989 Determining anisotropic real-analytic conductivities by boundary measurements *Commun. Pure Appl. Math.* **42** 1097–112
[63] Lionheart W R and Paridis K 2010 Finite elements and anisotropic EIT reconstruction, *Proc. Int. Conf. on Electrical Bioimpedance, J. Phys.: Conf. Ser.* **224** 012022
[64] Liu L 1997 Stability estimates for the two-dimensional inverse conductivity problem *PhD Thesis* University of Rochester
[65] Mueller J and Siltanen S 2003 Direct reconstructions of conductivities from boundary measurements *SIAM J. Sci. Comput.* **24** 1232–66
[66] Mueller J L and Siltanen S 2012 Linear and nonlinear inverse problems with practical applications *Comput. Sci. Eng.* **10** 351
[67] Mueller J L, Isaacson D and Newell J C 2001 Reconstruction of conductivity changes due to ventilation and perfusion from EIT data collected on a rectangular electrode array *Physiol. Meas.* **22** 97–106

[68] Nachman A I 1996 Global uniqueness for a two-dimensional inverse boundary value problem *Ann. Math.* **143** 71–96
[69] Nakamura G, Siltanen S, Tanuma K and Wang S 2005 Numerical recovery of conductivity at the boundary from the localized Dirichlet to Neumann map *Computing* **75** 197–213
[70] Nissinen A, Kolehmainen V and Kaipio J P 2010 Compensation of errors due to incorrect model geometry in electrical impedance tomography *J. Phys.: Conf. Ser.* **224** 012050
[71] Nissinen A, Kolehmainen V and Kaipio J P 2011 Compensation of modelling errors due to unknown domain boundary in electrical impedance tomography *IEEE Trans. Med. Imaging* **30** 231–42
[72] Siltanen S, Mueller J and Isaacson D 2000 An implementation of the reconstruction algorithm of A. Nachman for the 2D inverse conductivity problem *Inverse Problems* **16** 681–99
[73] Siltanen S and Tamminen J P 2013 Reconstructing conductivities with boundary corrected D-bar method *J. Inverse Ill-Posed Probl.* at press (doi:10.1515/jip-2013-0042)
[74] Sun Z and Uhlmann G 2003 Anisotropic inverse problems in two dimensions *Inverse Problems* **19** 1001–10
[75] Sylvester J 1990 An anisotropic inverse boundary value problem *Commun. Pure Appl. Math.* **43** 201–32
[76] Sylvester J and Uhlmann G 1987 A global uniqueness theorem for an inverse boundary value problem *Ann. Math.* **125** 153–69
[77] Zou Y and Guo Z 2003 A review of electrical impedance techniques for breast cancer detection *Med. Eng. Phys.* **25** 79–90